Correlations between valence electron concentration and the phase stability, intrinsic strength, and deformation mechanism in fcc multicomponent alloys

Yan-Xin Guo, Hai-Le Yan,* Nan Jia,† Bo Yang, Zongbin Li, and Liang Zuo

Key Laboratory for Anisotropy and Texture of Materials (Ministry of Education), School of Material Science and Engineering, Northeastern University, Shenyang 110819, China

(Received 22 September 2023; revised 23 November 2023; accepted 14 December 2023; published 5 January 2024)

Valence electron concentration (VEC) is a crucial parameter affecting the structure and mechanical properties of materials. Nevertheless, the influence of VEC in multicomponent alloys remains muddy. Here, the correlations between VEC and phase stability, intrinsic mechanical strength, and deformation mechanism are revealed by investigating six equiatomic CoNiM (M = Ti, V, Cr, Mn, Fe, and Cu) alloys with VEC ranging from 7.7 to 10.0. As VEC increases, the ground-state structure evolves from bcc to hcp and ultimately to fcc. Both elastic moduli and ideal tensile strength increase initially and then decrease with increasing VEC, i.e., an inverted parabolic trend, which arises due to the orbital-filling effect of valence electrons. We highlight that a medium VEC (∼8.3) has superior intrinsic strength at a full filling of the bonding state but an empty antibonding state. Furthermore, a strong link between intrinsic strength and the energy difference between bcc and fcc ($\Delta E_{\mathrm{fcc}\rightarrow\mathrm{bcc}}$) is built. The stacking fault (SF) energy γ_{sf} roughly increases with VEC except for in CoNiCr; this correlation is inherited from the energy difference between fcc and hcp. The dependence of intrinsic deformation energy barriers on VEC follows that of $\Delta E_{\mathrm{fcc}\rightarrow\mathrm{bcc}}$ since both are linked to the bonding strength. Depending on orientation, dislocation slip (SL) and SF can co-occur in the alloys with low VEC while SL and twinning (TW) coexist in those with high VEC. Both competition between SF or TW and SL and competition between SF and TW are dictated by γ_{sf}. This work unveils relations between VEC and phase stability, intrinsic strength, and deformation mechanisms and could provide some useful information for designing novel multicomponent alloys.

DOI: 10.1103/PhysRevB.109.024102

I. INTRODUCTION

Valence electron concentration (VEC) serves as a key parameter that significantly affects the phase structure [1–3] and the mechanical [4–6] and functional [7–10] performance of materials. In $NbCr_2$ [1] and $(FeCoNi)_3V$ [3] alloys, VEC is recognized as the dominant factor in controlling phase structure. At low VEC, $(FeCoNi)_3V$ prefers a hexagonal structure, while an ordered cubic structure becomes the favorable phase with the increase in VEC. For mechanical properties, a famous case is TiC_xN_{1-x}, where the system with VEC of ∼8.4 per cell exhibits the highest hardness [4,11]. Besides, superconductivity and the Invar effect were also reported to rely on VEC [9]. Nowadays, tuning VEC has been developed as a key strategy in tailoring the structure and properties of materials.

During the past decade, multicomponent alloys, also known as high- or medium-entropy alloys, have garnered significant attention due to their innovative design concept and remarkable mechanical and functional performance, such as high strength-ductility synergy [12–15], excellent radiation [16], catalytic performance [17,18], and corrosion and oxidation properties [19–21]. In analogy to conventional materials, the impact of VEC on structures and mechanical properties of multicomponent alloys is also non-negligible [22–31]. Guo *et al.* [23] discovered that at room temperature the AlCoCrCuFeNi alloys possess the single body-centered cubic (bcc) phase with VEC < 6.8, the dual phase with a mixed face-centered cubic (fcc) and bcc with 6.8 ⩽ VEC ⩽ 8.0, and the single fcc phase when VEC > 8.0. Chen *et al.* [27] reported that by decreasing or increasing VEC, the phase structures can be tailored to be bcc or fcc, respectively. For mechanical properties, it is argued that by changing VEC, the inherent ductility of refractory multicomponent alloys can be remarkably modified [29]. Besides, Rao *et al.* [30] discovered that $Fe_{34.2}Mn_{12.1}Co_{33.5}Ni_{12.3}Cu_{7.9}$ with a VEC of 8.7, which is identical to that of the classical $Fe_{65}Ni_{35}$ Invar alloy [9], also exhibits the Invar effect. These efforts significantly enhance our understanding of the influence of VEC on multicomponent alloys.

Nevertheless, the relations between VEC and the phase structures and mechanical performance, as well as underlying mechanisms, remain unclear in the fcc multicomponent alloys. In particular, the link between VEC and the deformation mechanism has never been established. Specifically, the following VEC-associated critical issues are still unaddressed: (i) Quantitative differences in phase stabilities of fcc, bcc, and hexagonal close-packed (hcp) affected by VEC are unclear. This knowledge is of utmost importance for a highly efficient design of phase structure in multicomponent alloys. (ii) The correlations between VEC and intrinsic strength, including elastic moduli and ideal tensile strength, as well as underlying mechanisms, remain unknown. The low yield

*yanhaile@mail.neu.edu.cn
†jian@atm.neu.edu.cn

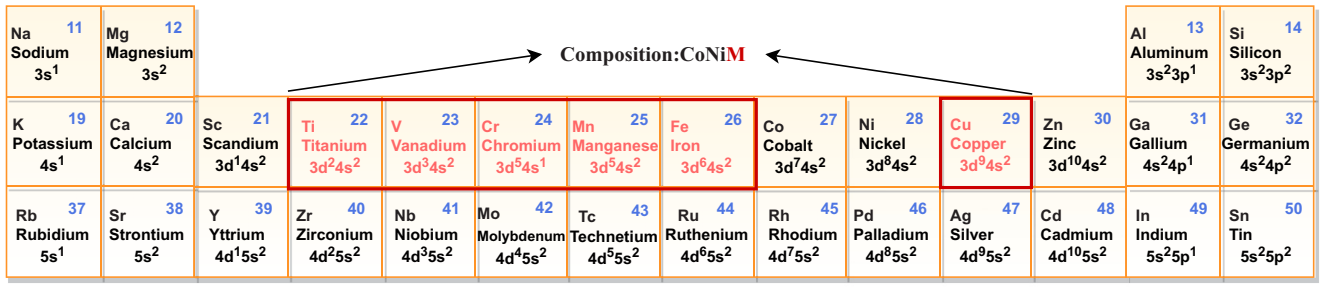

FIG. 1. Distribution of the M element in the studied CoNiM multicomponent alloys.

strength is one of the key obstacles to rendering the practical application of fcc multicomponent alloys. Clarifying the link between VEC and intrinsic strength might open a door to increasing the intrinsic strength of multicomponent alloys. (iii) The relation between VEC and the activation of deformation modes, such as dislocation slip, deformation twinning, and deformation-induced phase transitions, is unexplored. The plastic deformation ability of materials is majorly decided by the activation of deformation modes. Thus, uncovering the relation between VEC and deformation modes could be useful for the design of novel multicomponent alloys.

To bridge these knowledge gaps, the phase structures, intrinsic mechanical properties, electronic structures, and deformation mechanisms of a series of CoNiM multicomponent alloys are systematically studied by first-principles calculations. Herein, the M element is covered $3d$ transitional elements (M = Ti, V, Cr, Mn, Fe, and Cu, as highlighted in Fig. 1) to achieve a wide VEC ranging from 7.7 to 10.0. First, the lattice stabilities of the CoNiM alloys in the fcc, bcc, and hcp structures are systematically studied (Sec. III A). The relations between VEC and the energy difference among various phases are explored. Second, the elastic moduli and ideal tensile strength of the CoNiM alloys with the fcc structure are evaluated (Sec. III B). The dependences of intrinsic strengths on VEC as well as underlying mechanisms are discussed. Third, the generalized stacking fault energy curves (γ surface) are calculated (Sec. III C). The VEC dependences of stacking fault energy, intrinsic and effective energy barriers of dislocation slip, deformation twinning, and stacking fault (or stress-induced fcc $\rightarrow$ hcp phase transition), and activation of deformation modes are elucidated and discussed.

II. COMPUTATIONAL METHODOLOGY

A. Total energies of chemically disordered multicomponent alloys

Total energies of chemically disordered multicomponent alloys were calculated by using the exact muffin-tin orbit (EMTO) method [32–36] in combination with coherent potential approximation (CPA) [37]. The Kohn-Sham equation was solved within the scalar-relativity approximation and the soft-core scheme. The exchange-correlation energy was described with the generalized gradient approximation (GGA) in the Perdew-Burke-Ernzerhof (PBE) parametrization [38]. The s, p, d, and f orbitals were employed to treat the muffin-tin basis set. The Green's function was calculated for 32 complex energy points around valence states. The full charge density technique was applied for an accurate calculation of total energy [39]. The first Brillouin zone was sampled with uniform Monkhorst-Pack [40] k-point meshes of $21 \times 21 \times 21$ for bcc and fcc and $21 \times 21 \times 17$ for hcp, respectively. The paramagnetic state was simulated by the disordered local moment model [41].

B. Mechanical properties and stacking fault energy

Independent elastic constants were determined by using the strain-energy method (Appendix A 1) [42]. The Young's modulus E and shear modulus G for isotropic polycrystalline materials were estimated by using the Voigt-Reuss-Hill algorithm (Appendix A 2) [35]. The ideal tensile stress-strain curves of the fcc structure along [110] were calculated by the strain-energy method [43–45]. During the calculations, a series of uniaxial tensile strains ε, ranging from 0 to 0.09 with an interval of 0.01, were applied along [110], while the vectors perpendicular to [110] were fully relaxed under the conserved volume. The tensile stress $\sigma(\varepsilon)$ under the strain ε can be determined by the total energies of the strained lattices with the following relation:

$$\sigma(\varepsilon) = \frac{1+\varepsilon}{\Omega}\frac{\partial E(\varepsilon)}{\partial \varepsilon}, \tag{1}$$

where $E(\varepsilon)$ is the total energy per atom under strain ε and Ω is the volume per atom of the system. The generalized stacking fault energy curves of the fcc CoNiM alloys for $[11\bar{2}]$ shear on the $\{111\}$ plane were calculated by an alias shear of a periodic supercell lattice [46,47]. A 12-atom supercell structural model with six $\{111\}$ layers was adopted. The γ surface can be calculated by using the following relation:

$$\gamma \text{ surface} = \frac{E_{(x,y)} - E_0}{A_{(111)}}, \tag{2}$$

where E_0 and $E_{(x,y)}$ are the total energies of the system before and after slip, respectively, and $A_{(111)}$ is the area of the $\{111\}$ slip plane of the supercell.

C. Electronic structure

The electronic structure was calculated by using the Vienna *ab initio* simulation package (VASP) [48]. The energy convergence criterion and the plane-wave cutoff energy were set to be 10^{-5} and 600 eV, respectively. The PBE parametrization of the GGA was employed to describe the exchange-correlation function [38,49]. The electron-ion interactions were described by the projector augmented wave (PAW) pseudopotential

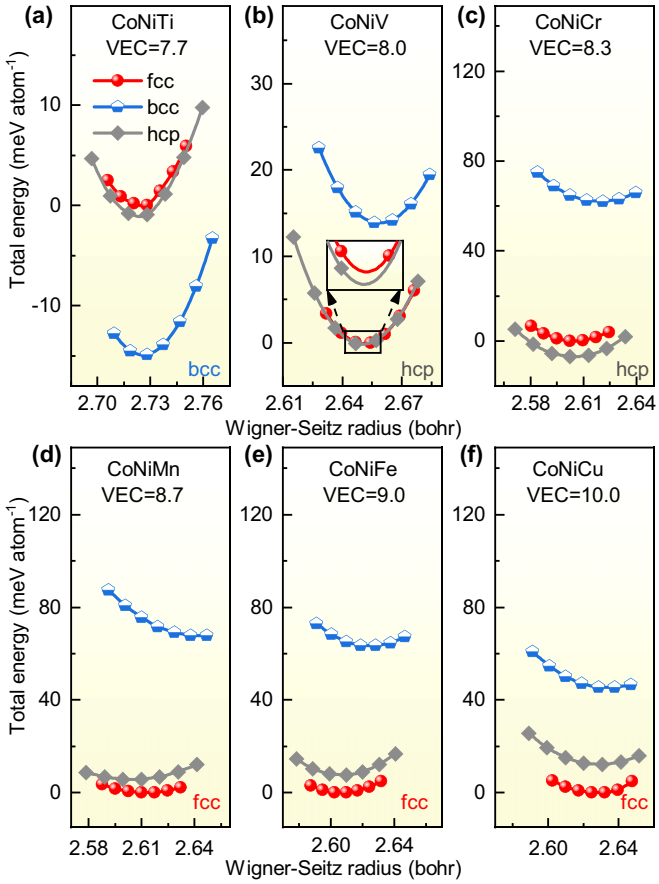

FIG. 2. Comparison of the total energies of the studied CoNiM alloys with the bcc, fcc, and hcp structures plotted as a function of the Wigner-Seitz radius. (a) CoNiTi, (b) CoNiV, (c) CoNiCr, (d) CoNiMn, (e) CoNiFe, and (f) CoNiCu. For a better illustration, the total energies of various structures are normalized with the minimum energy of the fcc structure. The inset in (b) is an enlarged image of the region indicated by the solid box.

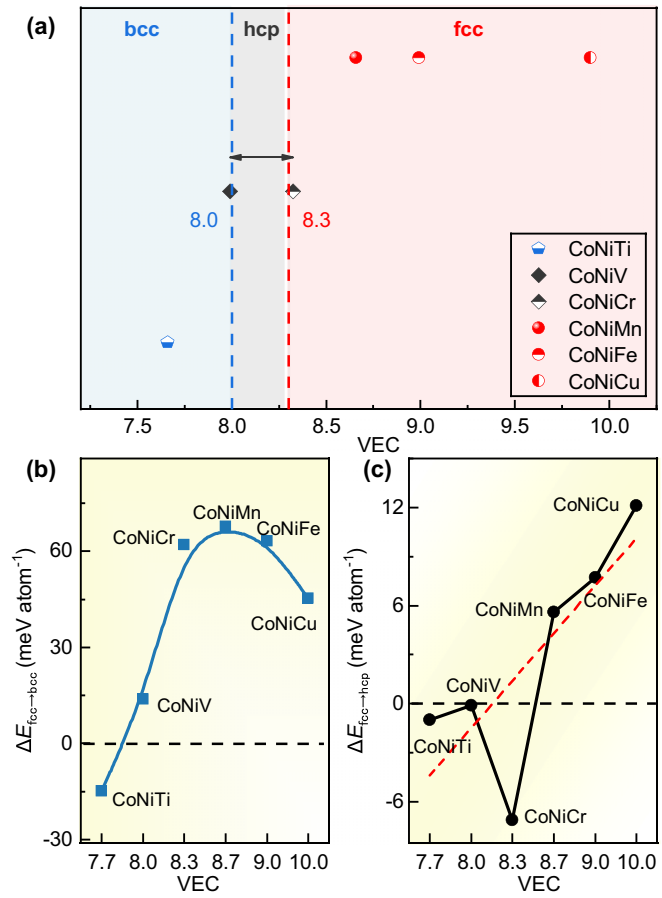

FIG. 3. VEC dependences of the ground-state structure and the energy difference between different structures. (a) Ground-state structure vs VEC. (b) $\Delta E_{fcc\rightarrow bcc}$ vs VEC. (c) $\Delta E_{fcc\rightarrow hcp}$ vs VEC. The red dashed line in (c) is to guide the eye.

approach. The chemical disorder was simulated by using the special quasirandom structure (SQS) approach as implemented in Alloy Theoretic Automated Toolkit (ATAT) [50]. The range of atom pair correlations is up to second-nearest neighbors. For the CoNiM alloys with the fcc structure, a 108-atom supercell, consisting of 36 atoms for each of Co, Ni, and M, was utilized. The Brillouin zone sampling was performed by the Monkhorst-Pack scheme with a $3 \times 3 \times 3$ k-point mesh. The projected crystal orbital Hamilton population (COHP) was determined by using Local Orbital Basis Suite Towards Electronic-Structure Reconstruction (LOBSTER) software [51,52]. The basis function sets of $3d$, $4s$, and $4p$ orbitals for all elements were considered.

III. RESULTS AND DISCUSSION

A. Phase stability

Figures 2(a)–2(f) display the total energies of the CoNiM (M = Ti, V, Cr, Mn, Fe, and Cu) alloys with the fcc, bcc, and hcp structures. Here, the paramagnetism treated by using the disordered local moment approach [41] is considered since the CoNi-based multicomponent alloys typically exhibit paramagnetism at room temperature [53–56]. We see that CoNiTi, with the lowest VEC (VEC = 7.7), exhibits a preference for the bcc structure with a thermodynamic advantage of ~15 (meV atom^{-1}) compared with the fcc and hcp structures [Fig. 2(a)]. With increasing VEC, the most favorable structure shifts towards the hcp type, as exhibited in CoNiV, with a VEC of 8.0 [Fig. 2(b)], and CoNiCr, with a VEC of 8.3 [Fig. 2(c)]. Remarkably, for CoNiV, the thermodynamic stabilities of the fcc and hcp phases are almost identical with an energy difference of less than 1 (meV atom^{-1}). With further increase in the VEC, the most stable structure becomes the fcc type, as shown in CoNiMn with a VEC of 8.7 [Fig. 2(d)], CoNiFe with a VEC of 9.0 [Fig. 2(e)], and CoNiCu with a VEC of 10.0 [Fig. 2(f)]. These findings highlight a strong correlation between VEC and the phase structure. More clearly, as plotted in Fig. 3(a), the CoNiM alloys with lower VEC favor the bcc structure (VEC < 8.0), while those with higher VEC prefer the fcc structure (VEC > 8.3); meanwhile, the alloys with a medium VEC tend to adopt the hcp structure.

This result, i.e., the result that a high VEC favors the fcc structure while a low VEC prefers the bcc structure, is consistent with the observations of Guo *et al.* [23] and Chen *et al.* [27]. It is known that the VEC dependence of the crystal structure is ascribed to the distinct distribution features of the electron density of state (DOS) of different structures [22,57].

Normally, the perfect bcc structure possesses a bimodal DOS of d orbitals, while the fcc and hcp structures exhibit a unimodal DOS. At low VEC, the filling in bimodal DOS leads to a more negative electronic band energy compared with the filling in unimodal DOS. Inversely, at high VEC, the filling in unimodal DOS corresponds to a lower band energy. Besides, one may note that the ground-state structure of CoNiCr [Fig. 2(c)] is determined to be hcp, aligning well with the results of a previous theoretical study [58]. Nevertheless, this result seems to contradict the experimental observation of a single fcc structure at room temperature [59]. The Gibbs free energy calculation shows that the fcc phase gradually evolves into being the favorable phase in the thermodynamics compared with the hcp phase in CoNiCr with elevated temperature. Details of the calculations are given in the Supplemental Material [60] (see also Refs. [35,61–66] therein). Moreover, very recently, a local hcp structure has been detected in CoNiCr at 77 K [58].

To quantitatively clarify the difference in stabilization by VEC in different phases, the correlations between VEC and the energy differences between various phases are investigated. In Fig. 3(b), we display the total energy difference between the bcc and fcc structures ($\Delta E_{\mathrm{fcc}\to\mathrm{bcc}}$) defined by $E_{\mathrm{bcc}} - E_{\mathrm{fcc}}$ plotted as a function of VEC. As VEC increases, $\Delta E_{\mathrm{fcc}\to\mathrm{bcc}}$ increases rapidly followed by a slight decrease. In the subsequent text, for simplicity, we refer to this tendency as an "inverted parabolic trend," although the right side of this curve is obviously higher than the left side. Notably, $\Delta E_{\mathrm{fcc}\to\mathrm{bcc}}$ of CoNiCr, CoNiMn, and CoNiFe with medium VEC possess the largest positive values ($\sim$60 meV atom^{-1}). In contrast, CoNiTi, with the lowest VEC, shows a negative $\Delta E_{\mathrm{fcc}\to\mathrm{bcc}}$ (-15 meV atom^{-1}). Figure 3(c) illustrates the VEC dependence of the energy difference between the hcp and fcc structures ($\Delta E_{\mathrm{fcc}\to\mathrm{hcp}}$) defined by $E_{\mathrm{hcp}} - E_{\mathrm{fcc}}$. With the exception of CoNiCr, $\Delta E_{\mathrm{fcc}\to\mathrm{hcp}}$ shows a roughly linear increasing trend with increasing VEC, as indicated by the dashed line. This result implies that a higher VEC tends to stabilize the fcc phase over the hcp phase. The large negative deviation of CoNiCr is believed to be associated with the special magnetoresistive frustration effect of Cr [67].

B. Mechanical properties

To clarify the relation between VEC and intrinsic strength, the elastic moduli and ideal tensile strength of the CoNiM alloys are calculated. Herein, for all the studied alloys, the fcc structure is examined, even though some of the alloys are not fcc at the ground state. The reasons for this selection are twofold. First, most of the studied CoNiM alloys, including CoNiCr and CoNiV, possess a single fcc phase in experiments at room temperature [54,55,68,69]. Therefore, studying the fcc structure is more meaningful to guide experiments. Second, by focusing on the same structure, the results of different CoNiM alloys can be directly compared, which facilitates unveiling the hidden links between VEC and intrinsic mechanical properties.

1. Elastic moduli

In Table I, we list the determined lattice constant a_0 and independent elastic constants of the CoNiM alloys along with those of CoNiCr, CoNiMn, and CoNiFe reported in the literature [70,71]. Calculation details are given in Appendix A 1. We see that the determined a_0 and elastic constants of CoNiCr, CoNiMn, and CoNiFe are in good agreement with the previous results. For all the alloys, the elastic constants satisfy the Born-Huang elastic stability criteria [72], i.e., $C_{11} > 0$, $C_{44} > 0$, $C_{11} + 2C_{12} > 0$, and $C_{11} > C_{12}$. It is known that for cubic crystals, the tetragonal shear modulus C' defined by $(C_{11} - C_{12})/2$ serves as an indicator of dynamic instability, resulting from the coupling of shear modes and leading to a breaking of crystal symmetry [73]. In Fig. 4(a), we plot the relation between C' and VEC. We see that the variation of C' as a function of VEC displays an inverted parabolic trend, mirroring that of $\Delta E_{\mathrm{fcc}\to\mathrm{bcc}}$ [Fig. 3(b)]. This result in the CoNiM alloys is in good agreement with the observation in pure transition metals [57,74,75]. It suggests that for CoNiM alloys with fcc structure the dynamic stability is enhanced initially with an increase in VEC followed by a slight decrease.

TABLE I. VEC, lattice constant a_0, and independent elastic constant C_{ij} of fcc CoNiM (M = Ti, V, Cr, Mn, Fe, and Cu) paramagnetic alloys.

Alloy	VEC	a_0 (Å)	C_{11} (GPa)	C_{12} (GPa)	C_{44} (GPa)
CoNiTi	7.7	3.68	131.4	111.3	115.3
CoNiV	8.0	3.58	247.3	196.4	147.8
CoNiCr	8.3	3.52	298.2	204.0	179.4
		3.53[a]	290.1[a]	197.3[a]	175.9[a]
		3.52[b]	278.8[b]	188.8[b]	183.0[b]
CoNiMn	8.7	3.53	197.5	101.3	182.1
		3.53[b]	211.7[b]	116.4[b]	184.4[b]
CoNiFe	9.0	3.52	235.6	145.6	178.0
		3.53[b]	234.2[b]	144.2[b]	177.9[b]
CoNiCu	10.0	3.54	224.1	152.3	145.0

[a]Reference [70].
[b]Reference [71].

Figures 4(b), 4(c), and 4(d) show the VEC dependences of the isotropic shear modulus G, the isotropic Young's modulus E, and the bulk modulus B, respectively. Calculation details are described in Appendix A 2. Surprisingly, for all G, E, and B, their variations with VEC roughly follow the trend of C' [Fig. 4(a)], i.e., an inverted parabolic trend, as depicted by the dashed curves. This result suggests that the CoNiM alloys with high elastic moduli can be found at a medium VEC. Among the studied alloys, CoNiCr, with a VEC of 8.3, exhibits the highest combination of elastic moduli, namely $C' = 47.1$ GPa, $G = 105.0$ GPa, $E = 274.0$ GPa, and $B = 235.4$ GPa. One may note that the B values of CoNiMn and CoNiFe exhibit relatively large deviations from the inverted parabolic trend [highlighted by the dashed ellipse in Fig. 4(d)], which will be discussed later.

2. Ideal tensile strength

The ideal tensile strength is an indicator of inherent mechanical properties of materials, playing a crucial role in understanding a material's mechanical performance [76,77]. Figure 5(a) illustrates the ideal tensile stress-strain curves of the fcc CoNiM alloys along the [110] direction [70]. The

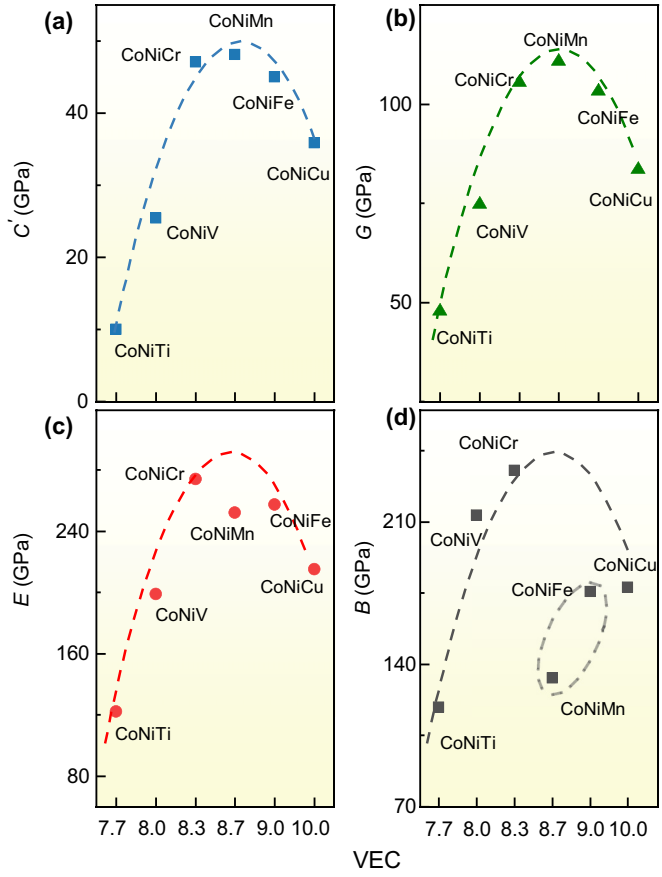

FIG. 4. Evolution of elastic moduli with respect to VEC. (a) Tetragonal shear modulus C', (b) isotropic shear modulus G, (c) isotropic Young's modulus E, and (d) bulk modulus B. The dashed inverted parabolic curves in (a)–(d) are plotted to guide the eye.

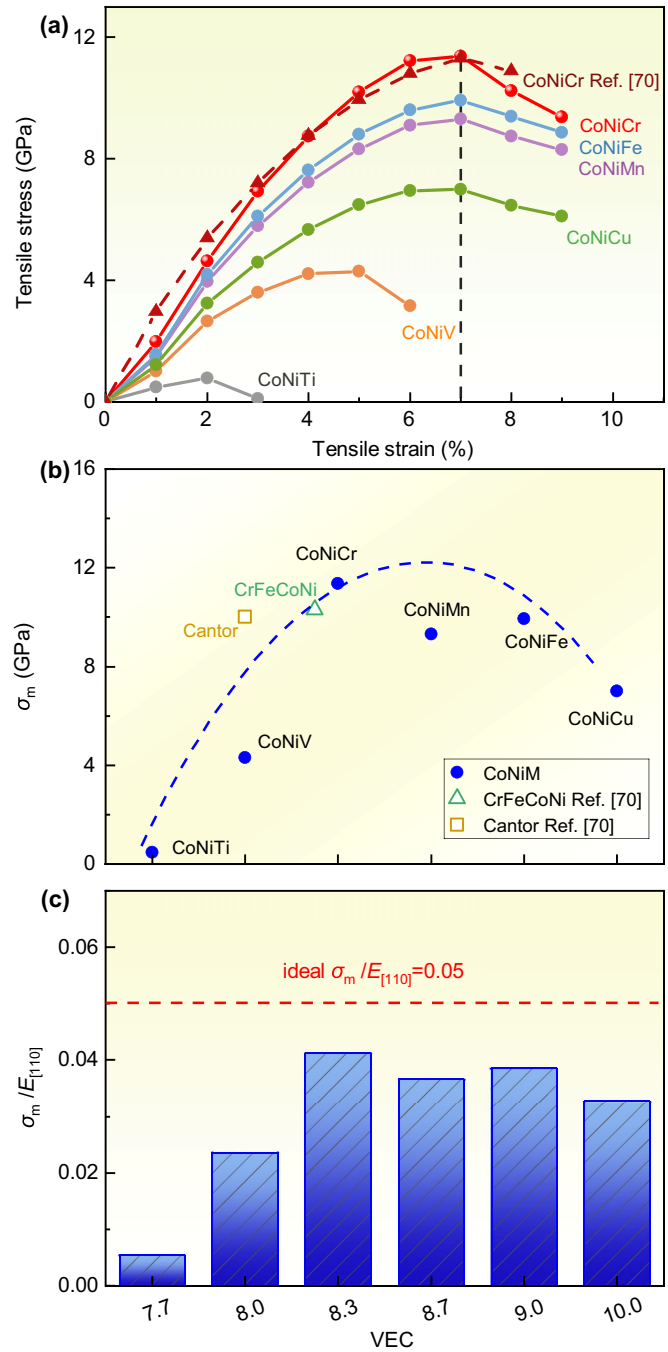

FIG. 5. Ideal tensile stress-strain curves of the CoNiM alloys. (a) Ideal tensile stress-strain curve along [110]. (b) Evolution of σ_m as a function of VEC. The dashed inverted parabolic curve is plotted to guide the eye. (c) Ratio between σ_m and $E_{[110]}$ with respect to VEC. One of the two sets of data for CoNiCr in (a) is extracted from Ref. [70], as are the data for the Cantor and CrFeCoNi alloys in (b).

reason for this selection is that [110] is the weakest direction of the fcc crystal. For comparison, the ideal tensile stress-strain curve of CoNiCr [70] is also included. The excellent agreement between our result and the previous report for CoNiCr evidences the reliability of our calculations. We see that CoNiCr exhibits the highest ideal tensile strength σ_m (11.3 GPa) at a maximum strain ε_m of ∼7%. In contrast, CoNiTi demonstrates the lowest σ_m (0.47 GPa) with ε_m of ∼2%. The lowest ε_m of CoNiTi could be attributed to the fact that this alloy is inherently unstable in the fcc configuration and tends to transform into the bcc structure [Fig. 2(a)].

In Fig. 5(b), we plot the relation between σ_m and VEC. Amazingly, we observe that with the increased VEC, σ_m exhibits an inverted parabolic trend. To validate the generality of this trend, the σ_m of two classical alloys, FeMnCoCrNi (the Cantor alloy) and CrFeCoNi [70], are also plotted. It is clear that despite the significant composition difference between these two alloys and the CoNiM alloys, they roughly follow the inverted parabolic relation between σ_m and VEC. Among the studied alloys, CoNiCr with a medium VEC (8.3) possesses the highest σ_m, which is even higher than those of the CrFeCoNi and Cantor alloys, although the configuration entropy of CoNiCr (1.1R) is smaller than that of the CrFeCoNi (1.4R) and Cantor (1.6R) alloys. This result provides us with an alternative viewpoint to understand the superior mechanical properties of CoNiCr in experiment [68]. Moreover, this finding implies that there exists a strong relation between VEC (rather than configuration entropy) and the intrinsic strength of the fcc multicomponent alloys. Besides, one may note that the σ_m of CoNiV is smaller than that of CoNiCr, which seems to contradict the experimental observations of a higher yield

stress of CoNiV [55,68]. This discrepancy may be associated with the neglected effects of local lattice distortion (LLD) and chemical short-range order (SRO) in this paper, which are believed to play key roles in the high yield strength of CoNiV [55]. The presence of prominent LLD in CoNiV leads to an atom strain field, which elastically interacts with the strain field of dislocations and provides pinning forces to the activation and movement of dislocations [55]. Moreover, the existence of SRO in CoNiV [78] could also act as a barrier to pinning dislocation, thus contributing to a high yield stress. A detailed discussion about the roles of LLD and SRO is given in the Supplemental Material [60] (see also Refs. [12,22,55,56,58,79–91] therein). In this paper, considering that LLD and SRO vary greatly in different CoNiM alloys, the effects of these two factors are omitted for a better illustration of the role of VEC.

In Fig. 5(c), we display the ratio between σ_m and Young's modulus E along [110] (i.e., $\sigma_m/E_{[110]}$) with respect to VEC. As a reference, the line of $\sigma_m/E_{[110]} = 0.05$, which is determined by assuming sinusoidal stress-strain behavior for a defined cell volume and is often used to estimate σ_m from $E_{[110]}$ [92], is also plotted. We find that the $\sigma_m/E_{[110]}$ values of all CoNiM alloys are smaller than 0.05. Among them, the alloys with medium VEC, such as CoNiCr, CoNiMn, and CoNiFe, are much closer to the line of 0.05 compared with those with low and high VEC. This observation further indicates that a medium VEC (∼8.3) is favorable to achieve a superior intrinsic strength.

From Figs. 4 and 5, we know that the VEC dependences of all the investigated intrinsic strengths, including C', E, G, B, and σ_m, exhibit the identical characteristic, i.e., an inverted parabolic trend. This finding provides us with useful information to tune the intrinsic strength of fcc multicomponent alloys. Furthermore, we note that the VEC dependences of intrinsic strengths are exactly the same as that of $\Delta E_{fcc\to bcc}$ [Fig. 3(b)]. In Figs. 6(a) and 6(b), we display the elastic moduli C', E, G, and B and σ_m with respect to $\Delta E_{fcc\to bcc}$. Clearly, a roughly linear relation between intrinsic strengths and $\Delta E_{fcc\to bcc}$ is observed. Thus $\Delta E_{fcc\to bcc}$ may also serve as an indicator of intrinsic strength. As is known, $\Delta E_{fcc\to bcc}$ can be routinely obtained by first-principles calculations. This provides an alternative guidance to design novel fcc multicomponent alloys.

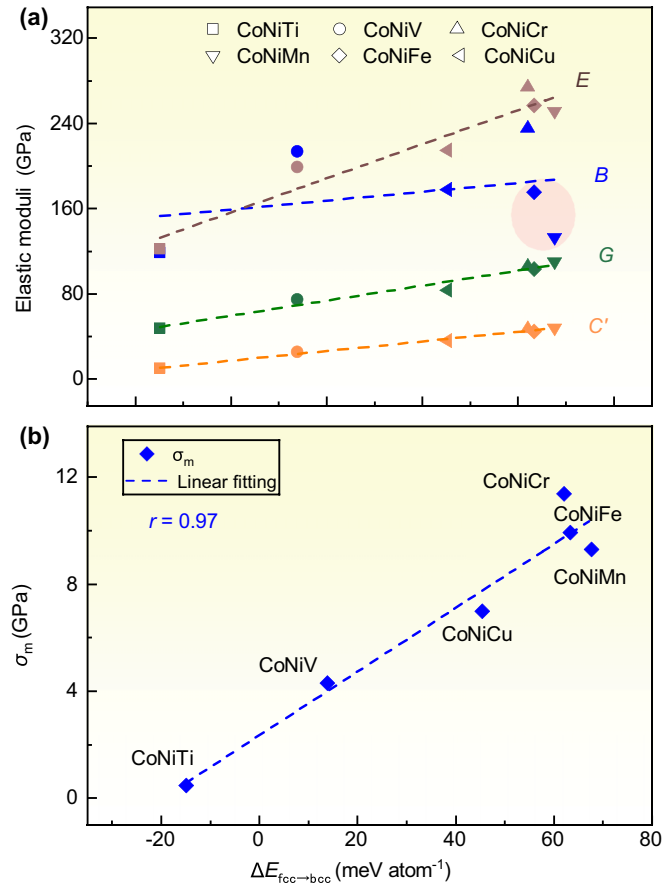

FIG. 6. Relation between intrinsic strength and $\Delta E_{fcc\to bcc}$. (a) C', G, E, and B. (b) σ_m.

3. *Mechanism of the VEC dependence of intrinsic strength*

To clarify the correlation between VEC and intrinsic strength, the crystal orbital Hamilton population (COHP) of the CoNiM alloys is investigated. For each alloy, a 108-atom supercell constructed by using the SQS method [50] was built to mimic chemical disorder. For simplicity but without the loss of generality, herein, nonmagnetism was considered. Figures 7(a)–7(f) display the mean COHP curves of various first-nearest-neighboring chemical bonds of the CoNiM alloys. Remarkably, the mean COHP curves of the studied CoNiM alloys share similar features, as depicted in Fig. 8(a). At low energy, there exists a substantial bonding state with −COHP greater than 0. As the energy rises, the nonbonding state with −COHP equaling 0 appears. With further elevated energy, the antibonding state with −COHP less than 0 is observed. These bonding and antibonding states around the Fermi level E_F should be majorly associated with the 3d orbital electrons of transition metal elements (i.e., Co, Ni, and M) [93,94].

Despite the similar COHP frames of various CoNiM alloys, their E_F positions with respect to the bonding and antibonding states are greatly different. Figure 8(b) highlights the position of E_F of the different CoNiM alloys in the aligned schematic COHP diagrams plotted with the information of the calculated COHP curves. Note that the illustration in Fig. 8(b) is different from that in Fig. 7, in which the COHP curves are aligned with their normalized E_F (i.e., $E - E_F = 0$). For CoNiTi and CoNiV, E_F is located in the region of the bonding state. Notably, from CoNiTi to CoNiV, E_F moves up and approaches the nonbonding state gradually, leading to a higher filling degree of the bonding state in CoNiV compared with CoNiTi [highlighted by the light blue areas in Fig. 8(b)]. For CoNiCr, E_F climbs to the region of the antibonding state but is very close to the nonbonding state. As for CoNiMn, CoNiFe, and CoNiCu, their E_F continues to move upwards and further away from the nonbonding state, resulting in an increasing filling degree of the antibonding states [highlighted by the light red areas in Fig. 8(b)].

As is known, electron occupation in the bonding state is favorable to enhancing the strength of chemical bonding, while the occupation of the antibonding state tends to weaken

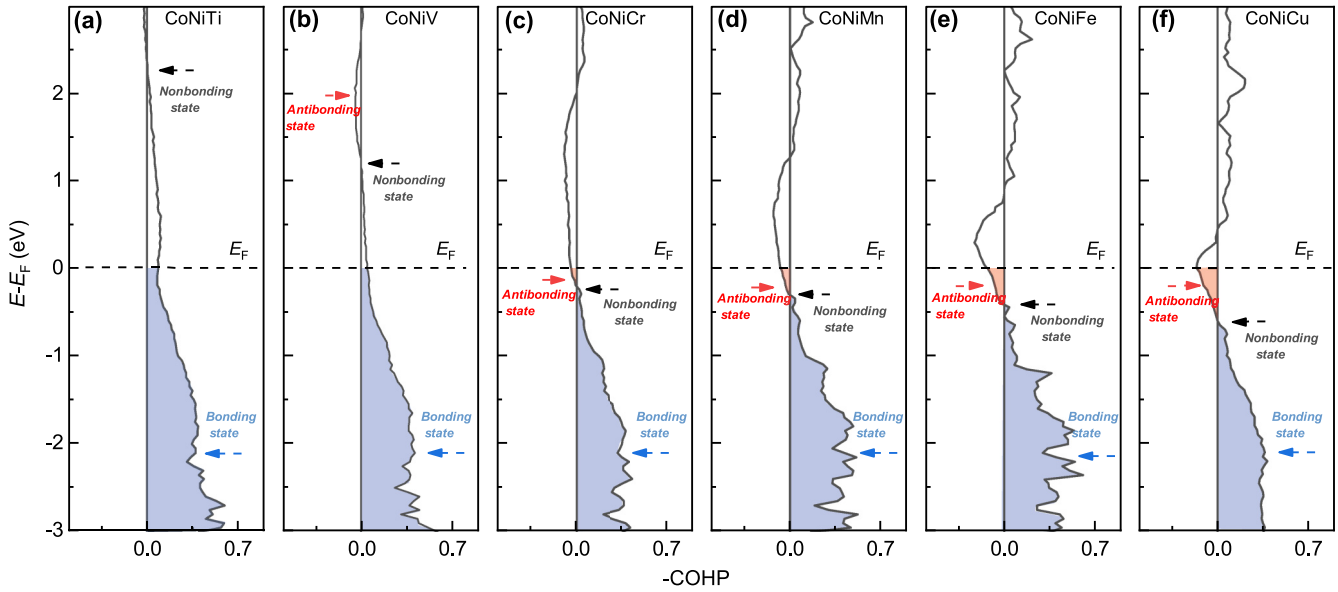

FIG. 7. COHP curves of the CoNiM alloys. (a) CoNiTi, (b) CoNiV, (c) CoNiCr, (d) CoNiMn, (e) CoNiFe, and (f) CoNiCu.

the bonding strength. From CoNiTi to CoNiV to CoNiCr, the bonding state is gradually filled up (even with partial occupation of the antibonding state in CoNiCr). This explains the enhanced elastic moduli and σ_m of the CoNiM alloys with the M element from Ti to Cr. From CoNiMn to CoNiFe to CoNiCu, more and more antibonding states are filled. This accounts for their gradually weakened mechanical strength. Thus the band-filling effect of valence electrons should be responsible for the various observed property trends with the inverted parabolic relation. To quantitatively elucidate the band-filling degree of various CoNiM alloys, the energy integration of COHP up to E_F (ICOHP), an indicator describing bonding strength [51,52], is calculated. The result is shown in Fig. 9. We see that the absolute value of ICOHP (|ICOHP|) of the CoNiM alloys increases first and then decreases with the M element going from Ti to Cu, in good agreement with the above analysis. Besides, in addition to bonding strength, the band-filling effect also governs the value of $\Delta E_{fcc\rightarrow bcc}$ [57]. This accounts for the established link between $\Delta E_{fcc\rightarrow bcc}$ and intrinsic strength (Fig. 6).

From the above discussion, it is evident that the position of E_F with respect to the bonding and antibonding states would be the key factor affecting the degree of band filling and then deciding the intrinsic mechanical strength. Specifically, with the variation of the M element from Ti to Cu, E_F moves upwards continuously from the bonding state to the antibonding state, leading to an increase initially and then a decrease in bonding strength, which is responsible for the variation in mechanical properties of the CoNiM alloys. We now discuss the reason behind the gradually raised E_F from CoNiTi to CoNiCu. As is known, E_F represents the highest energy of the occupied electron state, and the integration of the electronic DOS up to E_F equals the valence electron number of the system. Thus, when the variation in the DOS structure is limited, the number of valence electrons of the system, in other words, VEC, would be the key factor in deciding E_F [94,95]. For the studied CoNiM alloys, the increased valence electron number of the M elements from Ti ($3d^2 4s^2$) to Cu ($3d^{10} 4s^1$) accounts well for the varying E_F of the CoNiM alloys, which suggests that VEC would be the key factor deciding the position of

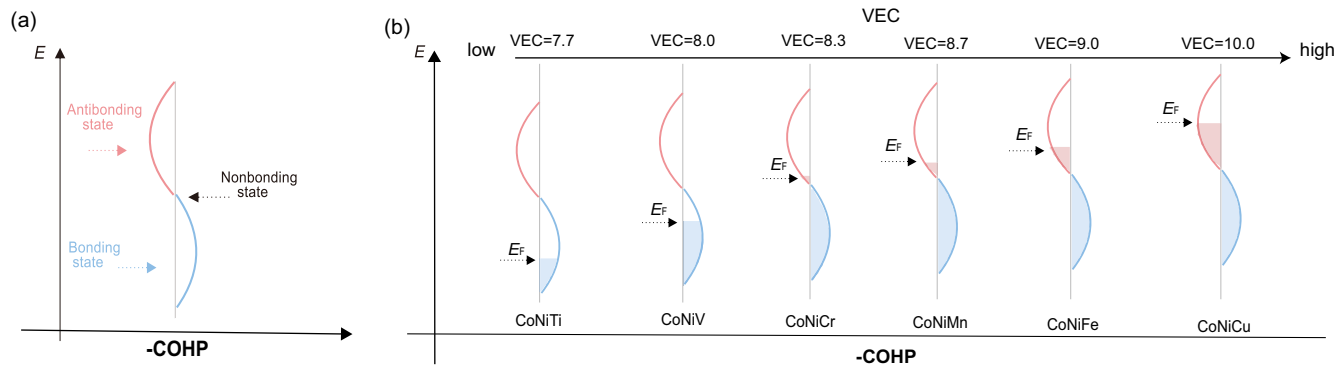

FIG. 8. Schematic diagram of COHP of the CoNiM alloys. (a) Schematic COHP diagram. (b) COHP of the CoNiM alloys with highlighted E_F.

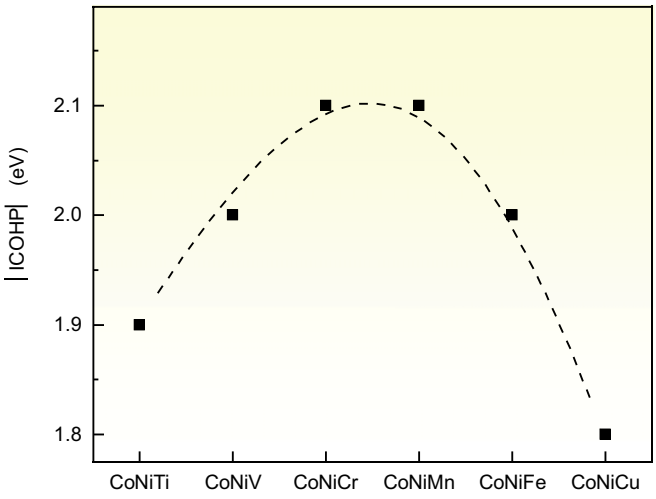

FIG. 9. |ICOHP| of CoNiM.

E_F in various CoNiM alloys. This is reasonable since all the studied CoNiM alloys have fcc structure and the various M elements have similar valence electron configurations (characterized by an open $3d$ shell), and thus the DOS structures of the studied CoNiM alloys would share similar features. Although the differences in atomic radius and electronegativity (and also other factors) of the M elements could also tune the position of E_F by affecting the DOS structure, their roles would be relatively limited compared with that of VEC.

We now discuss the possible reason for the anomalies in B in CoNiMn and CoNiFe, i.e., the relatively large negative deviation compared with the inverted parabolic relation [Fig. 4(d)]. Herein, a factor Δr characterizing the expansion or contraction of lattice volume during the formation of solid solution is introduced. The definition of Δr is as follows:

$$\Delta r = r_0 - \bar{r} = \sqrt[3]{\frac{3}{16\pi}}\, a_0 - \sum_{i=1}^{3} \frac{r_i}{3}, \tag{3}$$

where r_0 is the average atomic radius of the CoNiM alloys and $\bar{r}$ represents the mean of the atomic radii r_i of the Co, Ni, and M elements. Figure 10(a) displays the Δr determined for various CoNiM alloys. Amazingly, except for CoNiMn and CoNiFe, the Δr possess negative values. This observation shows that during the formation of the solid solution, the mean atomic radii of CoNiMn and CoNiFe are elongated while those of the other alloys are shortened. As is known, the bulk modulus B is very sensitive to lattice volume [62]. The expansion of the lattice typically weakens bonding strength. This might be the reason for the relatively large negative deviation in B in CoNiMn and CoNiFe. In Fig. 10(b), we plot the atomic magnetic moments of the CoNiM alloys. We see that the atomic magnetic moments in CoNiMn and CoNiFe are obviously prominent compared with other alloys. The atomic moments of Mn and Fe in CoNiMn and CoNiFe are determined to be 2.24 and 2.36 μ_B atom^{-1}, respectively, which values are even larger than those in the pure metals (0.58 μ_B atom^{-1} for Mn [96] and 1.32 μ_B atom^{-1} for Fe [97]). As is known, the magnetic moment significantly affects the lattice volume of a crystal [62]. Generally, a large magnetic moment tends to expand the volume of the lattice. Thus the

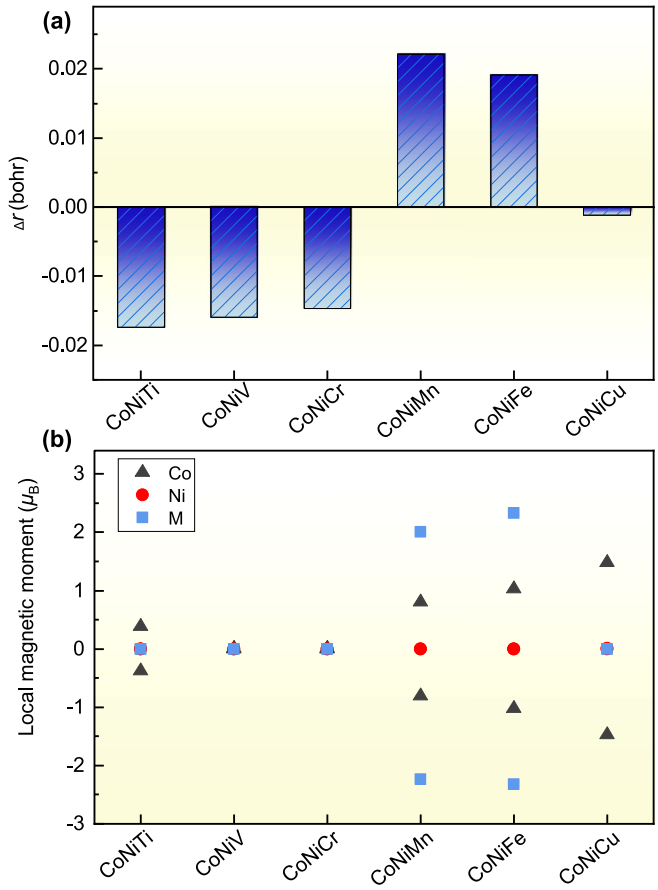

FIG. 10. Variation of mean atomic radius during the formation of solid solution and local magnetic moment of the CoNiM alloys. (a) Δr defined by $r_0 - \bar{r}$, where r_0 is the average atomic radius of the CoNiM alloy and $\bar{r}$ represents the mean of the atomic radii r_i of the Co, Ni, and M elements. (b) Local atomic magnetic moments of Co, Ni, and M in the paramagnetic CoNiM alloys.

large magnetic moment of Mn and Fe in CoNiMn and CoNiFe could be the reason for their positive Δr and, further on, relatively small B.

C. Plastic deformation mechanism

We now focus on the relation between VEC and the activation of the plastic deformation mode. The mechanical performance of metallic materials is greatly shaped by the plastic deformation mechanism [98–100]. A trade-off between strength and ductility is generally inevitable when dislocation slip occurs solely. By contrast, introducing deformation twinning or stress-induced phase transformation can reliably break this dilemma. For the fcc alloys, the activation of deformation mechanisms can be effectively predicted from the generalized planar fault energy (GPFE) curve [101].

1. Generalized stacking fault energy

Figure 11(a) depicts the three typical GPFE curves of the $\{111\}$ close-packed plane shearing along $\langle 11\bar{2}\rangle$. For the perfect fcc structure, the stacking sequence of $\{111\}$ is $\cdots$ ABCABC $\cdots$. When a Shockley partial dislocation moves along 1/6 $[11\bar{2}]$ (V_1) on a certain (111) plane, an

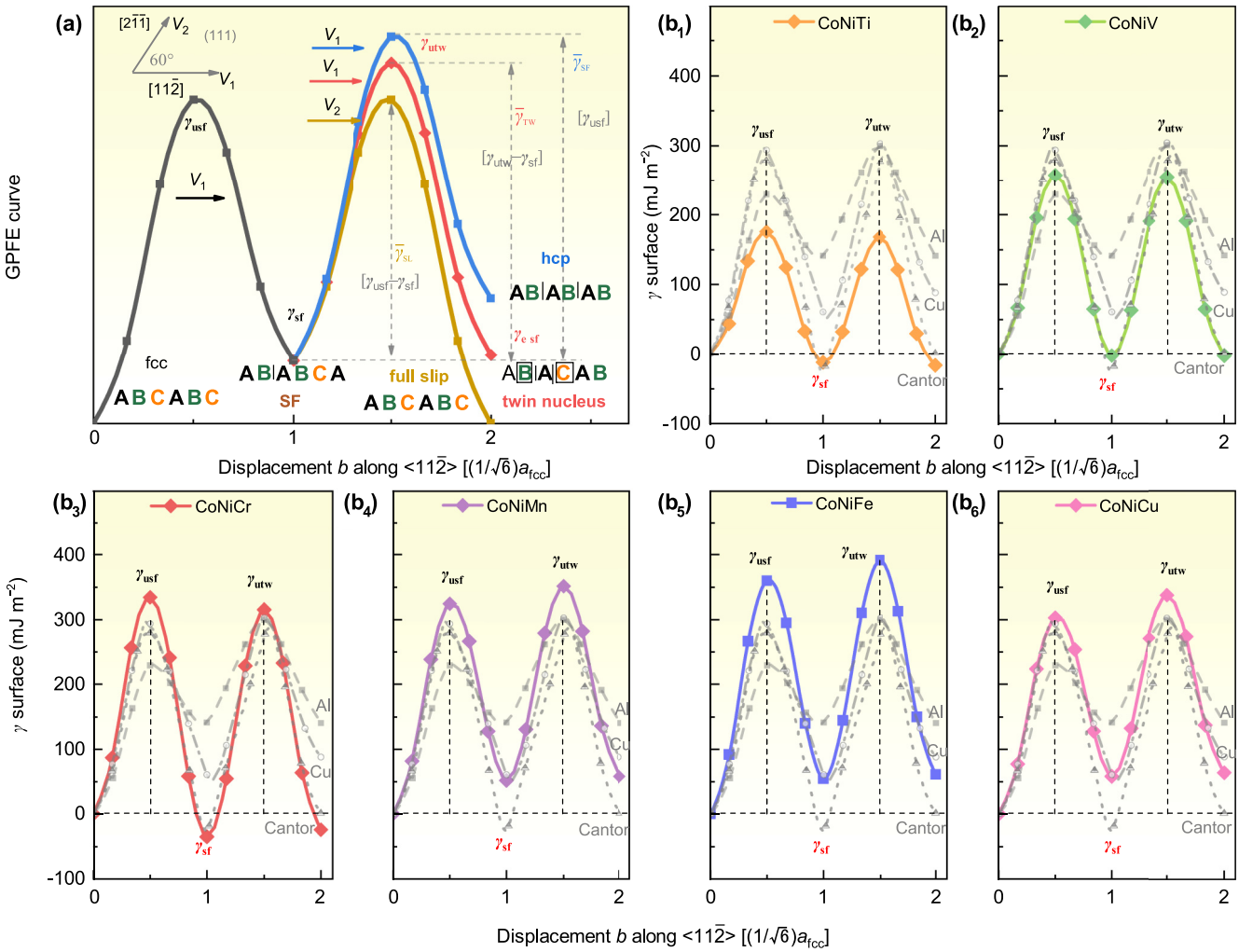

FIG. 11. GPFE curves and γ surfaces of the fcc CoNiM alloys for $\langle 11\bar{2}\rangle$ alias shear on the $\{111\}$ plane. (a) Three typical GPFE curves of the fcc alloys. (b_1)–(b_6) γ surfaces of CoNiTi, CoNiV, CoNiCr, CoNiMn, CoNiFe, and CoNiCu. For comparison, γ surfaces of three typical fcc alloys, i.e., Al, Cu, and Cantor alloy that possess high (142 mJ m^{-2}) [104], medium (43 mJ m^{-2}) [104], and low (-18 mJ m^{-2}) [105] γ_{sf}, respectively, are included.

intrinsic stacking fault (SF) with a stacking sequence of $\cdots$ AB|ABCA$\cdots$ ("|" represents the SF plane) appears. The energy barrier ($b = 0.5$) and valley ($b = 1.0$) are the so-called unstable SF energy γ_{usf} and the stable intrinsic SF energy γ_{sf}, respectively. Starting from this existing SF, there are three travel routes for $\{111\}$, corresponding to three common deformation modes of fcc metals, i.e., dislocation slip, deformation twinning, and the stress-induced fcc $\rightarrow$ hcp phase transition. (i) If the $\{111\}$ plane moves continuously but along $1/6$ $[2\bar{1}\bar{1}]$ (V_2), the SF disappears with a stacking of $\cdots$ ABCABC$\cdots$, corresponding to a full dislocation. (ii) When another partial dislocation is activated on a consecutive $\{111\}$ plane along $1/6$ $[11\bar{2}]$ (V_1), the stacking sequence becomes $\cdots$ A$\boxed{B}$|A|$\boxed{C}$AB$\cdots$, and hence a three-layer twin nucleus with the interfaces of $\boxed{B}$ and $\boxed{C}$ is generated. The energy barrier ($b = 1.5$) and valley ($b = 2.0$) are the unstable twinning fault energy γ_{utw} and extrinsic SF energy γ_{esf}, respectively. Conventionally, the energy evolution from the perfect fcc and passing through the intrinsic SF to the extrinsic SF is referred to as the generalized stacking fault energy or γ surface. (iii) When partial dislocations regularly occur on every other $\{111\}$ plane, the stacking becomes $\cdots$ AB|AB|AB$\cdots$, and hence an hcp nucleus is formed. Normally, the energy evolution along routes (i) and (iii) can be approximately evaluated from the γ surface, which is due to the fact that the impact of SF on both lattice strain and charge redistribution is limited on the adjacent two $\{111\}$ planes for typical fcc alloys [102]. Specifically, for dislocation slip, the energy variation (dark yellow curve in Fig. 11(a) is symmetric to that of the intrinsic SF [black curve in Fig. 11(a)], which is reasonable as these two processes, in fact, correspond to the leading and trailing partial dislocations, respectively. As for the stress-induced fcc $\rightarrow$ hcp phase transition, the energy variation [light blue curve in Fig. 11(a)] typically is equal to a rigid shift of that of the intrinsic SF with a magnitude of γ_{sf} [103].

In Figs. 11(b_1)–11(b_6), we display the γ surfaces of the six studied CoNiM alloys along with those of three typical fcc alloys with a high, medium, and low γ_{sf}, respectively, i.e., Al (142 mJ m^{-2}) [104], Cu (43 mJ m^{-2}) [104], and Cantor

(-18 mJ m^{-2}) [105]. We see that for the alloys with low VEC, including CoNiTi [Fig. 11(b_1)], CoNiV [Fig. 11(b_2)], and CoNiCr [Fig. 11(b_3)], γ_{usf} is near to (or even larger than) γ_{utw} and γ_{sf} is close to zero (or even negative). This shape of the γ surface is similar to that of the Cantor alloy. Nevertheless, for the alloys with high VEC, such as CoNiMn [Fig. 11(b_4)], CoNiFe [Fig. 11(b_5)], and CoNiCu [Fig. 11(b_6)], their γ surfaces are more like those of Al and Cu. Specifically, γ_{usf} is obviously smaller than γ_{utw}, and γ_{sf} is greatly larger than zero. These results imply that there might be a link between VEC and the γ surface in fcc multicomponent alloys. In what follows, we will focus on exploring the relations between VEC and γ_{sf}, intrinsic and effective energy barriers, and the activation of deformation modes.

2. Intrinsic stacking fault energy

The correlation between γ_{sf} and VEC is first investigated due to the key role of γ_{sf} in the plastic deformation mechanism. For completeness, in addition to extracting it from the γ surface, γ_{sf} is reevaluated by using the first-order axial interaction model (AIM) with the neglect of the transformation strain energy [86,106,107]. In the picture of the AIM, γ_{sf} is estimated by

$$\gamma_{sf} = \frac{2\Delta E_{fcc\to hcp}}{A_{(111)}}, \tag{4}$$

where $A_{(111)}$ is the unit area of the {111} plane. In Fig. 12(a), we compare the γ_{sf} of the CoNiM alloys determined by AIM with those extracted from the γ surface. It is evident that the γ_{sf} values calculated using these two approaches align well with each other. From Eq. (4), one knows that γ_{sf} is dictated by two parameters, i.e., $\Delta E_{fcc\to hcp}$ and $A_{(111)}$, where the latter solely relies on lattice constant a_0. Thus a natural question arises as to which factor is the dominant one in deciding γ_{sf}. To address this issue, in Figs. 12(b_1) and 12(b_2), we plot the γ_{sf} of the CoNiM alloys as a function of $\Delta E_{fcc\to hcp}$ and a_0, respectively. Remarkably, γ_{sf} increases in a roughly linear manner with respect to $\Delta E_{fcc\to hcp}$ with a Pearson's correlation coefficient of as high as 0.96 [Fig. 12(b_1)]. In contrast, no clear pattern is seen in the a_0 vs γ_{sf} plot [Fig. 12(b_2)]. This result illustrates that $\Delta E_{fcc\to hcp}$, rather than a_0, decides the variation of γ_{sf} in the CoNiM alloys. In Fig. 12(c), we visualize the relation between VEC and γ_{sf}. As expected, following $\Delta E_{fcc\to hcp}$ [Fig. 3(c)], γ_{sf} is roughly linearly correlated with VEC except for in CoNiCr.

3. Intrinsic energy barrier

For any physical or chemical process, the energy barrier is a critical parameter because a prerequisite for the occurrence is a higher driving field against the energy barrier. In this section, the VEC dependences of intrinsic energy barriers (IEBs) of various deformation modes are investigated. As depicted in Fig. 11(a), IEBs of full dislocation slip (SL, $\overline{\gamma}_{SL}$), deformation twinning (TW, $\overline{\gamma}_{TW}$), and stacking fault or stress-induced fcc $\to$ hcp phase transition (SF, $\overline{\gamma}_{SF}$) can be calculated by

$$\overline{\gamma}_{SL} = \gamma_{usf} - \gamma_{sf}, \tag{5}$$

$$\overline{\gamma}_{TW} = \gamma_{utw} - \gamma_{sf}, \tag{6}$$

$$\overline{\gamma}_{SF} = \gamma_{usf}. \tag{7}$$

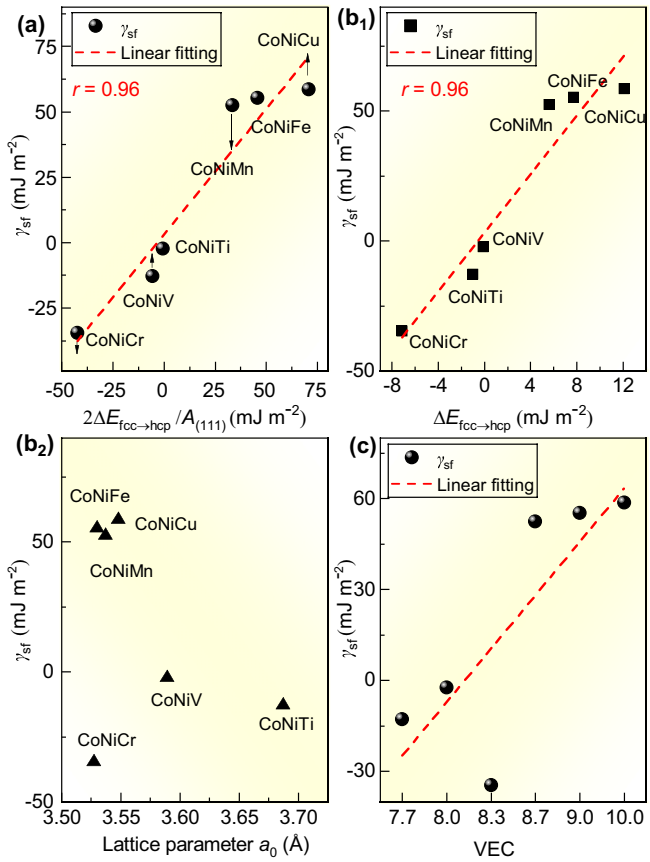

FIG. 12. Intrinsic stacking fault energy γ_{sf}. (a) Comparison of γ_{sf} determined by the AIM with those extracted from the γ_{sf} surface. (b_1) and (b_2) Relations between γ_{sf} and $\Delta E_{fcc\to hcp}$ (b_1) and between γ_{sf} and the equilibrium lattice constant a_0 (b_2). (c) Dependence of γ_{sf} on VEC.

Figures 13(a_1), 13(a_2), and 13(a_3) display the $\overline{\gamma}_{SL}$, $\overline{\gamma}_{TW}$, and $\overline{\gamma}_{SF}$ of the CoNiM alloys vs VEC, respectively. Amazingly, the IEBs $\overline{\gamma}_{SL}$, $\overline{\gamma}_{TW}$, and $\overline{\gamma}_{SF}$ all show an inverted parabolic trend with respect to VEC, which is exactly the same as the inverted parabolic trends of $\Delta E_{fcc\to bcc}$ [Fig. 3(b)], the elastic moduli (Fig. 4), and the ideal tensile strength [Fig. 5(b)]. In Figs. 13(b_1), 13(b_3), and 13(b_3), we plot $\overline{\gamma}_{SL}$, $\overline{\gamma}_{TW}$, and $\overline{\gamma}_{SF}$, respectively, vs $\Delta E_{fcc\to bcc}$ taken as an example. Clearly, $\overline{\gamma}_{SL}$, $\overline{\gamma}_{TW}$, and $\overline{\gamma}_{SF}$ all exhibit strongly linear correlations with $\Delta E_{fcc\to bcc}$. This result tells us that in addition to $\Delta E_{fcc\to hcp}$, which can greatly shape the deformation mechanism by deciding γ_{sf}, $\Delta E_{fcc\to bcc}$ should also play a non-negligible role in the activation of the deformation mechanism due to the strong link between it and the IEBs of various deformation modes.

We now discuss the mechanism behind the inverted parabolic correlation between IEBs and VEC. Herein, we take the IEB of SF as an example, i.e., from $\cdots$ ABCABC $\cdots$ to $\cdots$ AB|ABCA $\cdots$. As shown in Fig. 13(c), during the formation of an intrinsic SF, e.g., when layer C of {111} moves to the position of layer A, atom C′ in layer C should slip across between atoms B′ and B″ in the adjacent layer B. The IEB indeed corresponds to the configuration where atom C′ is exactly between atoms B′ and B″. During the movement of layer C, the spacing between atoms B′ and B″ in the adjacent layer B would be inevitably disturbed. In return, the bonding

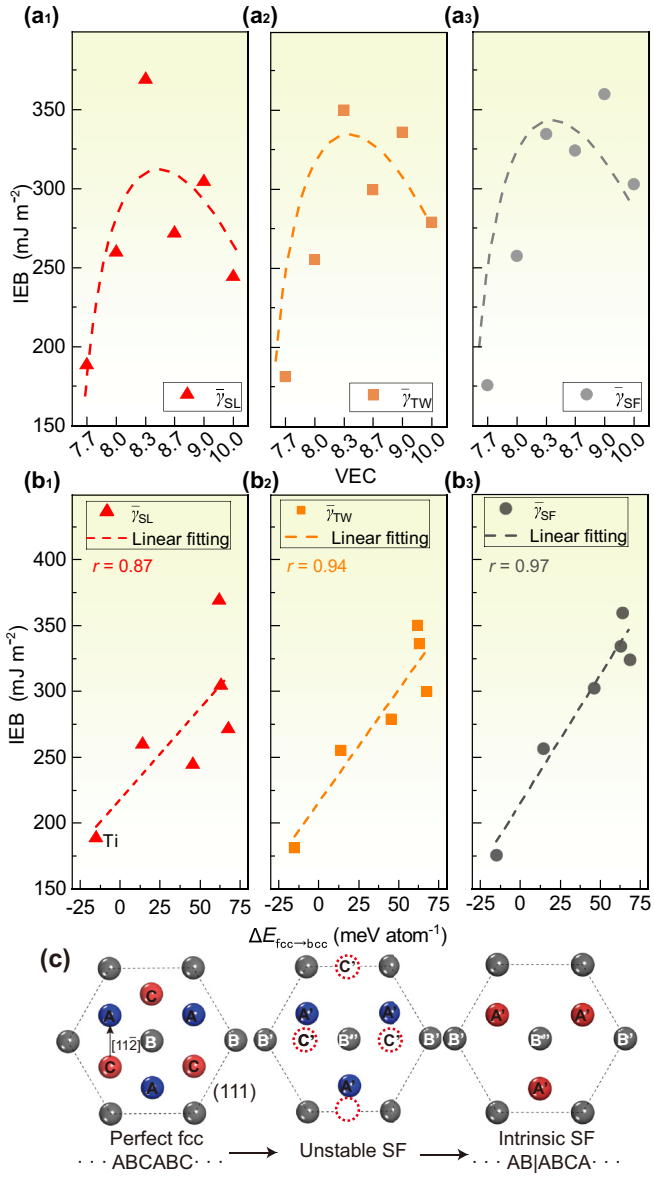

FIG. 13. Intrinsic energy barriers of dislocation slip $\overline{\gamma}_{\rm SL}$, deformation twinning $\overline{\gamma}_{\rm SL}$, and stacking fault $\overline{\gamma}_{\rm SF}$. ($a_1$)–($a_3$) Dependence of $\overline{\gamma}_{\rm SL}$, $\overline{\gamma}_{\rm TW}$, and $\overline{\gamma}_{\rm SF}$ on VEC. (b_1)–(b_3) Variation of $\overline{\gamma}_{\rm SL}$, $\overline{\gamma}_{\rm TW}$, and $\overline{\gamma}_{\rm SF}$ as a function of the energy difference between the bcc and fcc structures $\Delta E_{\rm fcc\to bcc}$. (c) Sketch of atom positions of layers A, B, and C during the formation of an intrinsic SF.

strength between atoms B′ and B″ would affect the formation of intrinsic SF. As revealed in Sec. III B 3, with the increase in VEC, the bonding strength is enhanced first with the increased filling fraction of the bonding state and weakens when the antibonding state is filled. This could be the reason for the inverted parabolic correlation between IEBs and VEC.

4. Effective energy barrier

Engineering materials are usually serviced in their polycrystalline form, in which different grains exhibit distinct crystallographic orientations. Apart from the IEB, the grain orientation with respect to the loading direction greatly affects the activation of the deformation mode, since SF, TW, and SL

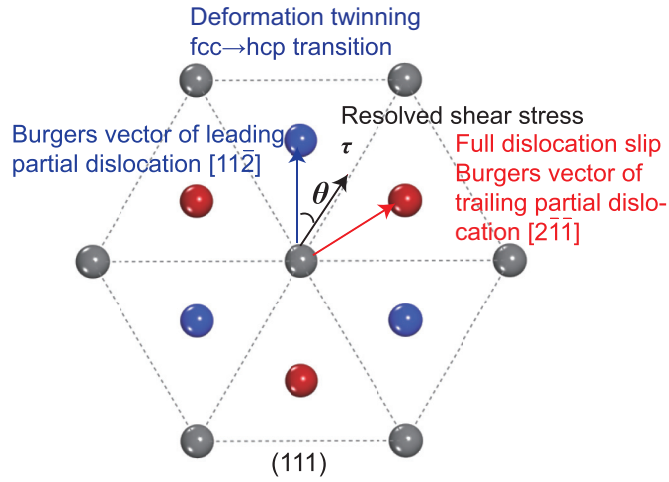

FIG. 14. Relative orientation of the Burgers vectors of partial dislocations for SF, the fcc → hcp transition, TW, and SL on (111) of the fcc structure. $\boldsymbol{\tau}$ indicates the resolved shear stress on (111). θ measures the deviation between $\boldsymbol{\tau}$ and the Burgers vector of the leading partial dislocation, which ranges from 0° to 60° according to the symmetry of the (111) planes of the fcc structure.

occur on specific and different crystal systems. For the fcc alloys, the angle deviation between the resolved shear stress $\boldsymbol{\tau}$ on {111} and the partial directions of various deformation modes takes a critical role in their competition. As shown in Fig. 14, the partial directions of TW and SF are identical (e.g., [11$\bar{2}$]), which is exactly the same as that of leading partial dislocation. By contrast, the partial direction of SL is 60° deviated from it (e.g., [2 $\bar{1}$ $\bar{1}$]). Under certain $\boldsymbol{\tau}$ on {111}, the effective energy barriers (EEBs) for SL, TW, and SF can be calculated by

$$\overline{\gamma}_{\rm SL}(\theta) = \frac{\overline{\gamma}_{\rm SL}}{\cos(60^\circ - \theta)} = \frac{\gamma_{\rm usf} - \gamma_{\rm sf}}{\cos(60^\circ - \theta)}, \tag{8}$$

$$\overline{\gamma}_{\rm TW}(\theta) = \frac{\overline{\gamma}_{\rm TW}}{\cos\theta} = \frac{\gamma_{\rm utw} - \gamma_{\rm sf}}{\cos\theta}, \tag{9}$$

$$\overline{\gamma}_{\rm SF}(\theta) = \frac{\overline{\gamma}_{\rm SF}}{\cos\theta} = \frac{\gamma_{\rm usf}}{\cos\theta}, \tag{10}$$

where θ, ranging from 0° to 60°, measures the deviation between $\boldsymbol{\tau}$ and the Burgers vector of leading partial dislocation [104]. Theoretically, the activated deformation mode should be the one with the lowest EEB.

Figure 15(a) displays the two-dimensional deformation mode map of the CoNiM alloys along with those of Al [104], Cu [104], and $Fe_{40}Mn_{40}Co_{10}Cr_{10}$ [105] as references. Herein, the projections of $\overline{\gamma}_{\rm SL}$, $\overline{\gamma}_{\rm TW}$, and $\overline{\gamma}_{\rm SF}$ on (111), i.e., $\overline{\gamma}^*_{\rm SL}$, $\overline{\gamma}^*_{\rm TW}$, and $\overline{\gamma}^*_{\rm SF}$, are adopted as the coordinate axes. Under this projection, the deformation mode map is clearly divided into three regions, that is, region SF (red), region TW (blue), and region SL (green). In each region, a single deformation mode, e.g., the SF mode in region SF, possesses the lowest EEB in the thermodynamics and thus tends to be activated [104]. In the map, each line represents the EEB trajectory of a given material with θ varying from 0° to 60°. We see that the EEB trajectories of CoNiTi and CoNiV are between those of Fe_{40} Mn_{40} Co_{10} Cr_{10} and Cu. For CoNiCr, its trajectory is the leftmost one among all the examined CoNiM alloys, which is

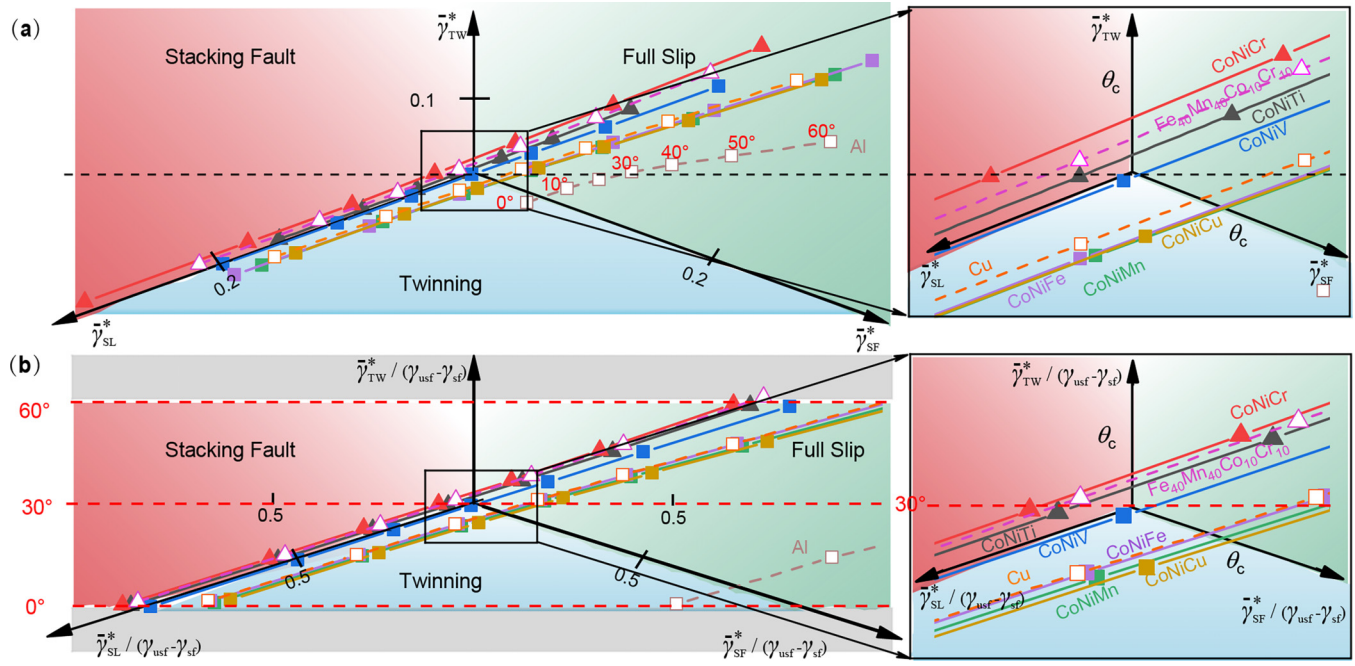

FIG. 15. Deformation mode maps. (a) Projected deformation mode map on (111). (b) Normalized deformation mode map scaled by $\gamma_{usf} - \gamma_{sf}$. The data for $Fe_{40}Mn_{40}Co_{10}Cr_{10}$ (pink-outlined white symbols) is extracted from Ref. [105], and those for Cu (orange-outlined white symbols), and Al (brown-outlined white symbols) are from Ref. [104].

attributed to this alloy having the smallest γ_{sf} [Fig. 12(a)]. As for CoNiMn, CoNiFe, and CoNiCu, their trajectories, residing between those of Cu and Al, almost coincide with each other. To gain deeper insight into these three alloys, the normalized deformation mode map with respect to the IEB of SL (i.e., $\gamma_{usf} - \gamma_{sf}$) is shown in Fig. 15(b). We see that the EEB trajectory of CoNiMn is located between those of CoNiFe and CoNiCu. Among all the CoNiM alloys, the trajectory of CoNiCu is the rightmost one, which is majorly ascribed to its having the highest γ_{sf} [Fig. 12(a)].

With the variation of θ, the EEB trajectories of all the studied CoNiM alloys are located in two regions. Thus, theoretically, depending on the grain orientation, two kinds of deformation modes might be activated in these alloys. In CoNiTi and CoNiCr, the EEB projections with small θ are located in region SF, while those with large θ enter region SL. By contrast, the EEB projections of CoNiV, CoNiFe, CoNiMn, and CoNiCu with small and large θ are within regions TW and SL, respectively. Thus, in these alloys, a co-occurrence of TW and SL could be possible.

Lastly, the relation between VEC and the competition between SF or TW and SL is discussed. In Fig. 16(a), we display the critical values of θ (denoted θ_c) for the transition of the deformation mode from SF (for CoNiCr and CoNiTi) or TW (for CoNiV, CoNiFe, CoNiMn, and CoNiCu) to SL plotted as a function of VEC. Interestingly, with the increase in VEC, θ_c exhibits a monotonically decreasing tendency except for in CoNiCr. Notably, this tendency is exactly opposite to that of γ_{sf} [Fig. 12(c)]. In Fig. 16(b), we visualize the relation between θ_c and γ_{sf}. A perfect linear correlation between θ_c and γ_{sf} is obtained with a Pearson's coefficient r of as high as -0.99. Thus γ_{sf} would be a key factor in deciding θ_c. Figure 16(c) shows the relation between θ_c and $\Delta E_{fcc\to hcp}$. Clearly, θ_c is also linearly correlated with $\Delta E_{fcc\to hcp}$ with a Pearson's coefficient r of -0.96, which is reasonable owing to the strong link between γ_{sf} and $\Delta E_{fcc\to hcp}$ [Fig. 12(b_1)].

It is identified above that at small θ, SF tends to be activated in the CoNiM alloys with low γ_{sf}, while TW prefers occurring in the alloys with high γ_{sf}. Before closing this section, we focus on the competition between SF and TW in the different CoNiM alloys. Figure 17(a) displays the EEB difference between the SF and TW modes for the CoNiM alloys plotted as a function of VEC. Herein, the same θ of 0° is taken as an example, which is representative since the θ dependence

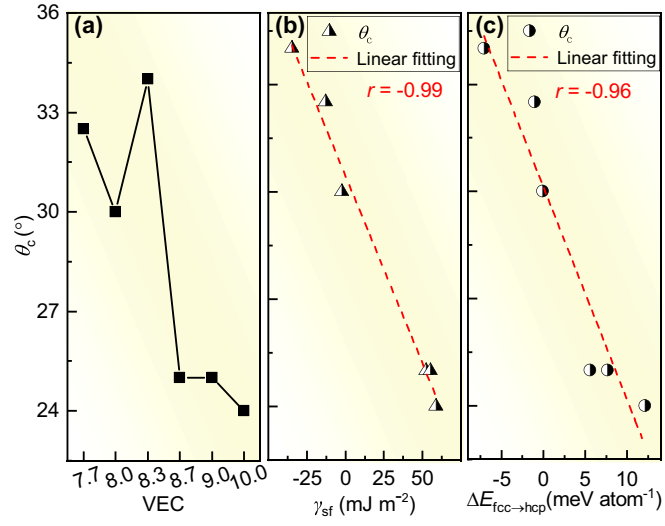

FIG. 16. Critical values of θ (denoted θ_c) for the transition of the deformation mechanism from SF (or TW) to SL: (a) θ_c vs VEC, (b) θ_c vs γ_{sf}, and (c) θ_c vs $\Delta E_{fcc\to hcp}$.

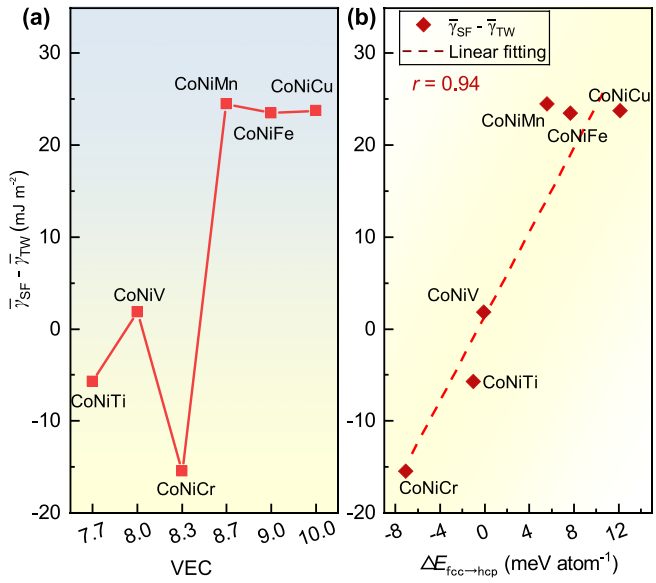

FIG. 17. Competition between SF and TW. (a) VEC dependence of the difference between $\overline{\gamma}_{SF}$ and $\overline{\gamma}_{TW}$. (b) Correlation between $\overline{\gamma}_{SF} - \overline{\gamma}_{TW}$ and $\Delta E_{fcc\to hcp}$. A negative value of $\overline{\gamma}_{SF} - \overline{\gamma}_{TW}$ implies a preference for SF, while a positive one indicates a preference for TW.

of EEBs for SF and TW are exactly the same [Eqs. (9) and (10)]. We see that the dependence of $\overline{\gamma}_{SF} - \overline{\gamma}_{TW}$ on VEC roughly follows the tendency of γ_{sf} [Fig. 12(c)]. In Fig. 17(b), we display the relation between $\overline{\gamma}_{SF} - \overline{\gamma}_{TW}$ and $\Delta E_{fcc\to hcp}$. Clearly, like the case of γ_{sf}, the difference between $\overline{\gamma}_{SF}$ and $\overline{\gamma}_{TW}$ is linearly correlated with $\Delta E_{fcc\to hcp}$ with a Pearson's coefficient r of 0.94. Thus $\Delta E_{fcc\to hcp}$ would play a dominant role in the competition between SF and TW.

IV. CONCLUSIONS

The correlations between VEC and the phase structures, elastic moduli, ideal tensile strengths, and generalized stacking fault energies of the equiatomic CoNiM (M = Ti, V, Cr, Mn, Fe, and Cu) multicomponent alloys with VEC ranging from 7.7 to 10.0 are systematically studied using first-principles calculations. The specific conclusions are as follows.

(i) With increasing VEC, the ground-state structure evolves from bcc (VEC $<$ 8.0) to hcp (8.0 $\leqslant$ VEC $\leqslant$ 8.3) and ultimately to fcc (VEC $>$ 8.3).

(ii) Both the elastic moduli C', E, G, and B and the ideal tensile strength σ_m show inverted parabolic trends with respect to VEC, i.e., a rapid increase at first followed by a slight decrease. This tendency is attributed to the orbital-filling effect of valence electrons. We emphasize that a medium VEC, such as 8.3 in CoNiCr, facilitates a superior intrinsic strength, since at a medium VEC a full filling of the bonding state but an empty antibonding state can be realized. Furthermore, a strong link between $\Delta E_{fcc\to bcc}$ and intrinsic strength is established. Additionally, a factor characterizing the change in the mean atomic radius during the formation of solid solution is introduced to explain the anomalies in B in CoNiMn and CoNiFe.

(iii) The stacking fault energy γ_{sf} is positively correlated with VEC except for in CoNiCr, and this positive correlation is inherited from the correlation between $\Delta E_{fcc\to hcp}$ and VEC. Depending on grain orientation, dislocation and stacking fault could coexist in the CoNiM alloys with low VEC, while dislocation and deformation twinning could co-occur in the alloys with high VEC. Both the competition between stacking fault (or twinning) and dislocation, characterized by the critical angle θ_c of deformation mode change, and the competition between stacking fault and twinning, indicated by $\overline{\gamma}_{SF} - \overline{\gamma}_{TW}$, are linearly correlated with γ_{sf}. Different from γ_{sf}, which follows the VEC tendency of $\Delta E_{fcc\to hcp}$, the intrinsic energy barriers of various deformation modes show an inverted parabolic trend, just like $\Delta E_{fcc\to bcc}$ and the intrinsic strength. The reason could be associated with the fact that all these factors are linked to the strength of chemical bonding. Thus, apart from $\Delta E_{fcc\to hcp}$, $\Delta E_{fcc\to bcc}$ should also play a non-negligible role in the activation of the deformation mechanism. The built links between various easily obtained materials parameters, e.g., VEC, $\Delta E_{fcc\to bcc}$, and $\Delta E_{fcc\to hcp}$, and the key factors associated with activation of the deformation mode, e.g., γ_{sf} and deformation energy barriers, supply a valid method to tune the deformation mechanism and further ductility.

In conclusion, this work unveils the correlation between VEC and phase structure, intrinsic strength, and deformation mechanism and is expected to provide some guidance for designing novel multicomponent alloys.

ACKNOWLEDGMENT

This work is supported by the National Natural Science Foundation of China (Grants No. 52371097 and No. 52274379), the Fundamental Research Funds for the Central Universities (Grant No. N2202015), and the 111 Project of China (Grants No. BP0719037 and No. B20029).

APPENDIX

1. Determination of independent elastic constants of cubic crystal by the strain-energy method

Independent elastic constants of cubic crystal, i.e., C_{11}, C_{12}, and C_{44}, are determined by using the strain-energy method [42]. First, the bulk modulus B is determined by fitting the energy vs volume curve with the Birch-Murnaghan fourth-order equation of state [61,108]. Second, a series of orthorhombic [Eq. (A1)] and monoclinic distortion strains [Eq. (A2)] with δ_m and δ_n varying from 0.00 to 0.05 with an interval of 0.01 are applied to the crystal, respectively.

$$\begin{pmatrix} 1+\delta_m & 0 & 0 \\ 0 & 1+\delta_m & 0 \\ 0 & 0 & \frac{1}{1-\delta_m^2} \end{pmatrix}, \tag{A1}$$

$$\begin{pmatrix} 1 & \delta_n & 0 \\ \delta_n & 1 & 0 \\ 0 & 0 & \frac{1}{1-\delta_n^2} \end{pmatrix}. \tag{A2}$$

The total energies of the distorted crystal, i.e., $\Delta E(\delta_m)$ and $\Delta E(\delta_n)$, are calculated by first-principles calculations. C' and C_{44} are then computed by fitting the total energies with respect to δ_m and δ_n as follows:

$$\Delta E(\delta_m) = 2VC'\delta_m^2 + O(\delta_m^4), \tag{A3}$$

$$\Delta E(\delta_n) = 2VC_{44}\delta_n^2 + O(\delta_n^4), \tag{A4}$$

where V is the lattice volume. Finally, C_{11} and C_{12} are derived from B and C' by solving the following two equations:

$$B = (C_{11} + 2C_{12})/3, \tag{A5}$$

$$C' = (C_{11} - C_{12})/2. \tag{A6}$$

2. Estimation of isotropic and anisotropic elastic moduli

The isotropic shear modulus G and Young's modulus E are calculated by using the Voigt-Reuss-Hill method [35,109], as follows:

$$G = \frac{1}{2}(G_V + G_R), \tag{A7}$$

$$E = \frac{9GB}{G + 3B}, \tag{A8}$$

where G_V and G_R are Voigt's and Reuss's shear modulus, respectively. For cubic crystals, G_V and G_R can be calculated by

$$G_V = \frac{1}{5}[(C_{11} - C_{12}) + 3C_{44}], \tag{A9}$$

$$G_R = \frac{5C_{44}(C_{11} - C_{12})}{3(C_{11} - C_{12}) + 4C_{44}}. \tag{A10}$$

The Young's modulus E and Poisson's ratio υ along the [109] direction [92] are computed by

$$E_{[110]} = \frac{\nu_{[110]}}{C_{12}}\left[C_{11}(C_{11}+C_{12}) - 2C_{12}^2\right], \tag{A11}$$

$$\nu_{[110]} = \frac{4C_{12}C_{44}}{C_{11}(C_{11} + C_{12} + 2C_{44}) - 2C_{12}^2}. \tag{A12}$$

[1] J. H. Zhu, P. K. Liaw, and C. T. Liu, Mater. Sci. Eng.: A **239-240**, 260 (1997).
[2] X. Jin, M. Marioni, D. Bono, S. M. Allen, and R. C. O'Handley, J. Appl. Phys. **91**, 8222 (2002).
[3] C. T. Liu, Int. Mater. Rev. **29**, 168 (1984).
[4] S. H. Jhi, J. Ihm, S. G. Louie, and M. L. Cohen, Nature (London) **399**, 132 (1999).
[5] S. Reeh, D. Music, M. Ekholm, I. A. Abrikosov, and J. M. Schneider, Phys. Rev. B **87**, 224103 (2013).
[6] K. Balasubramanian, S. V. Khare, and D. Gall, Acta Mater. **152**, 175 (2018).
[7] B. T. Matthias, Phys. Rev. **97**, 74 (1955).
[8] V. L. Moruzzi, Phys. Rev. B **41**, 6939 (1990).
[9] E. F. Wassermann and M. Acet, in *Magnetism and Structure in Functional Materials*, edited by A. Planes, L. Manosa, and A. Saxena, Springer Series in Materials Science Vol. 79 (Springer, Berlin, 2005), pp. 177–197.
[10] N. Rangaraju, J. A. Peters, and B. W. Wessels, Phys. Rev. Lett. **105**, 117202 (2010).
[11] S. H. Jhi, S. G. Louie, M. L. Cohen, and J. W. Morris Jr, Phys. Rev. Lett. **87**, 075503 (2001).
[12] Y. Zou, H. Ma, and R. Spolenak, Nat. Commun. **6**, 7748 (2015).
[13] N. Xiao, X. Guan, D. Wang, H. L. Yan, M. H. Cai, N. Jia, Y. D. Zhang, C. Esling, X. Zhao, and L. Zuo, Int. J. Miner. Metall. Mater. **30**, 1667 (2023).
[14] Z. He, Y. Guo, L. Sun, H.-L. Yan, X. Guan, S. Jiang, Y. Shen, W. Yin, X. Zhao, Z. Li, and J. Nan, Acta Mater. **243**, 118495 (2023).
[15] Z. He, N. Jia, H. Yan, Y. Shen, M. Zhu, X. Guan, X. Zhao, S. Jin, G. Sha, Y. Zhu, and C. T. Liu, Int. J. Plast. **139**, 102965 (2021).
[16] O. El-Atwani, N. Li, M. Li, A. Devaraj, J. K. S. Baldwin, M. M. Schneider, D. Sobieraj, J. S. Wróbel, D. Nguyen-Manh, S. A. Maloy, and E. Martinez, Sci. Adv. **5**, eaav2002 (2019).
[17] Y. N. Wang, H. Yang, Z. Zhang, X. Y. Meng, T. Cheng, G. W. Qin, and S. Li, J. Mater. Sci. Technol. **166**, 234 (2023).
[18] J. Hao, Z. Zhuang, K. Cao, G. Gao, C. Wang, F. Lai, S. Lu, P. Ma, W. Dong, T. Liu, M. Du, and H. Zhu, Nat. Commun. **13**, 2662 (2022).
[19] H. L. Liang, C. W. Tsai, and S. Guo, J. Alloys Compd. **883**, 160787 (2021).
[20] Y. L. Chou, Y. C. Wang, J. W. Yeh, and H. C. Shih, Corros. Sci. **52**, 3481 (2010).
[21] H. Luo, S. S. Sohn, W. Lu, L. Li, X. Li, C. K. Soundararajan, W. Krieger, Z. Li, and D. Raabe, Nat. Commun. **11**, 3081 (2020).
[22] C. Tandoc, Y. J. Hu, L. Qi, and P. K. Liaw, npj Comput. Mater. **9**, 53 (2023).
[23] S. Guo, C. Ng, J. Lu, and C. T. Liu, J. Appl. Phys. **109**, 103505 (2011).
[24] J. Wang, S. X. Bai, Y. Tang, S. Li, X. Y. Liu, J. H. Jia, Y. C. Ye, and L. A. Zhu, J. Alloys Compd. **868**, 159190 (2021).
[25] T. Yang, Y. L. Zhao, W. H. Liu, J. H. Zhu, J. J. Kai, and C. T. Liu, Mater. Res. Lett. **6**, 600 (2018).
[26] M. H. Tsai, K. Y. Tsai, C. W. Tsai, C. Lee, C. C. Juan, and J. W. Yeh, Mater. Res. Lett. **1**, 207 (2013).
[27] R. R. Chen, G. Qin, H. T. Zheng, L. Wang, Y. Q. Su, Y. L. Chiu, H. S. Ding, J. J. Guo, and H. Z. Fu, Acta Mater. **144**, 129 (2018).
[28] S. Sheikh, S. Shafeie, Q. Hu, J. Ahlström, C. Persson, J. Veselý, J. Zýka, U. Klement, and S. Guo, J. Appl. Phys. **120**, 164902 (2016).
[29] F. Y. Tian, L. K. Varga, N. X. Chen, J. Shen, and L. Vitos, J. Alloys Compd. **599**, 19 (2014).
[30] Z. Y. Rao, A. Cakir, O. Ozgun, D. Ponge, D. Raabe, Z. M. Li, and M. Acet, Phys. Rev. Mater. **5**, 044406 (2021).
[31] F. Y. Tian, L. K. Varga, N. X. Chen, J. Shen, and L. Vitos, Intermetallics **58**, 1 (2015).
[32] L. Vitos, Phys. Rev. B **64**, 014107 (2001).
[33] L. Vitos, I. A. Abrikosov, and B. Johansson, Phys. Rev. Lett. **87**, 156401 (2001).
[34] L. Vitos, J. O. Nilsson, and B. Johansson, Acta Mater. **54**, 3821 (2006).
[35] L. Vitos, *Computational Quantum Mechanics for Materials Engineers* (Springer, New York, 2007).
[36] S. Huang, W. Li, S. Lu, F. Y. Tian, J. Shen, E. Holmström, and L. Vitos, Scr. Mater. **108**, 44 (2015).
[37] S. Huang, X. Q. Li, H. Huang, E. Holmström, and L. Vitos, Mater. Chem. Phys. **210**, 37 (2018).

[38] J. P. Perdew, K. Burke, and M. Ernzerhof, Phys. Rev. Lett. **77**, 3865 (1996).

[39] L. Vitos, J. Kollar, and H. L. Skriver, Phys. Rev. B **55**, 13521 (1997).

[40] H. J. Monkhorst and J. D. Pack, Phys. Rev. B **13**, 5188 (1976).

[41] B. L. Gyorffyt, A. J. Pindors, J. Stauntonll, G. M. Stocks, and H. Winter, J. Phys. F: Met. Phys. **15**, 1337 (1985).

[42] S. H. Zhang and R. F. Zhang, Comput. Phys. Commun. **220**, 403 (2017).

[43] C. Jiang and S. G. Srinivasan, Nature (London) **496**, 339 (2013).

[44] X. Q. Li, S. Schönecker, J. J. Zhao, B. Johansson, and L. Vitos, Phys. Rev. B **87**, 214203 (2013).

[45] Q. Yu, L. Qi, R. K. Mishra, J. Li, and A. M. Minor, Proc. Natl. Acad. Sci. USA **110**, 13289 (2013).

[46] S. L. Shang, C. L. Zacherl, H. Z. Fang, Y. Wang, Y. Du, and Z. K. Liu, J. Phys.: Condens. Matter **24**, 505403 (2012).

[47] S. J. Zhao, G. M. Stocks, and Y. W. Zhang, Acta Mater. **134**, 334 (2017).

[48] G. Kresse and J. Furthmüller, Comput. Mater. Sci. **6**, 15 (1996).

[49] M. Ernzerhof and G. E. Scuseria, J. Chem. Phys. **110**, 5029 (1999).

[50] A. van de Walle, P. Tiwary, D. L. Olmsted, M. Asta, A. Dick, D. Shin, Y. Wang, L. Q. Chen, and Z. K. Liu, Calphad **42**, 13 (2013).

[51] S. Maintz, V. L. Deringer, A. L. Tchougreeff, and R. Dronskowski, J. Comput. Chem. **37**, 1030 (2016).

[52] R. Nelson, C. Ertural, J. George, V. L. Deringer, G. Hautier, and R. Dronskowski, J. Comput. Chem. **41**, 1931 (2020).

[53] K. Xiang, L. J. Chai, Y. Y. Wang, H. Wang, N. Guo, Y. L. Ma, and K. L. Murty, J. Alloys Compd. **849**, 156704 (2020).

[54] Z. Wu, H. Bei, F. Otto, G. M. Pharr, and E. P. George, Intermetallics **46**, 131 (2014).

[55] S. S. Sohn, A. Kwiatkowski da Silva, Y. Ikeda, F. Kormann, W. Lu, W. S. Choi, B. Gault, D. Ponge, J. Neugebauer, and D. Raabe, Adv. Mater. **31**, 1807142 (2019).

[56] B. Yin, S. Yoshida, N. Tsuji, and W. A. Curtin, Nat. Commun. **11**, 2507 (2020).

[57] P. Söderlind, O. Eriksson, J. M. Wills, and A. M. Boring, Phys. Rev. B **48**, 5844 (1993).

[58] C. Niu, C. R. LaRosa, J. Miao, M. J. Mills, and M. Ghazisaeidi, Nat. Commun. **9**, 1363 (2018).

[59] J. Miao, C. E. Slone, T. M. Smith, C. Niu, H. Bei, M. Ghazisaeidi, G. M. Pharr, and M. J. Mills, Acta Mater. **132**, 35 (2017).

[60] See Supplemental Material at http://link.aps.org/supplemental/10.1103/PhysRevB.109.024102 for computational details and results of the Gibbs free energies for the fcc, bcc, and hcp phases of CoNiCr and discussions about the effects of local lattice distortion and chemical short-range ordering on the intrinsic mechanical properties of fcc multicomponent alloys. The Supplemental Material also contains Refs. [12,22,35,55,56,58,61–66,79–91].

[61] V. L. Moruzzi, J. F. Janak, and K. Schwarz, Phys. Rev. B **37**, 790 (1988).

[62] D. Ma, B. Grabowski, F. Körmann, J. Neugebauer, and D. Raabe, Acta Mater. **100**, 90 (2015).

[63] H. C. Herper, E. Hoffmann, and P. Entel, Phys. Rev. B **60**, 3839 (1999).

[64] J. C. Slater, *Introduction to Chemical Physics* (Read Books, Redditch, England, 2011).

[65] Y. Ikeda, B. Grabowski, and F. Körmann, Mater. Charact. **147**, 464 (2019).

[66] F. Körmann, A. A. H. Breidi, S. L. Dudarev, N. Dupin, G. Ghosh, T. Hickel, P. Korzhavyi, J. A. Munoz, and I. Ohnuma, Phys. Status Solidi B **251**, 53 (2014).

[67] F. Walsh, M. Asta, and R. O. Ritchie, Proc. Natl. Acad. Sci. USA **118**, e2020540118 (2021).

[68] B. Gludovatz, A. Hohenwarter, K. V. Thurston, H. Bei, Z. Wu, E. P. George, and R. O. Ritchie, Nat. Commun. **7**, 10602 (2016).

[69] Y. Murakami, Y. Maeda, A. Kitada, K. Murase, and K. Fukami, Electrochem. Commun. **128**, 107057 (2021).

[70] X. Q. Li, S. Schönecker, W. Li, L. K. Varga, D. L. Irving, and L. Vitos, Phys. Rev. B **97**, 094102 (2018).

[71] H. H. Ge, H. Q. Song, J. Shen, and F. Y. Tian, Mater. Chem. Phys. **210**, 320 (2018).

[72] G. A. Alers and J. R. Neighbours, J. Appl. Phys. **28**, 1514 (1957).

[73] G. Grimvall, B. Magyari-Köpe, V. Ozoliņš, and K. A. Persson, Rev. Mod. Phys. **84**, 945 (2012).

[74] J. Friedel and C. M. Sayers, J. Phys. France **38**, 697 (1977).

[75] J. Friedel, J. Phys. Radium **16**, 829 (1955).

[76] A. Kelly, W. R. Tyson, and A. H. Cottrell, Philos. Mag. **15**, 567 (1967).

[77] L. Qi and D. C. Chrzan, Phys. Rev. Lett. **112**, 115503 (2014).

[78] X. Chen, Q. Wang, Z. Cheng, M. Zhu, H. Zhou, P. Jiang, L. Zhou, Q. Xue, F. Yuan, J. Zhu, X. Wu, and E. Ma, Nature (London) **592**, 712 (2021).

[79] F. Körmann and M. H. Sluiter, Entropy **18**, 403 (2016).

[80] H. Song, F. Tian, Q.-M. Hu, L. Vitos, Y. Wang, J. Shen, and N. Chen, Phys. Rev. Mater. **1**, 023404 (2017).

[81] Y. Ye, Y. Zhang, Q. He, Y. Zhuang, S. Wang, S. Shi, A. Hu, J. Fan, and Y. Yang, Acta Mater. **150**, 182 (2018).

[82] G. D. Samolyuk, Y. N. Osetsky, G. M. Stocks, and J. R. Morris, Phys. Rev. Lett. **126**, 025501 (2021).

[83] H. S. Oh, S. J. Kim, K. Odbadrakh, W. H. Ryu, K. N. Yoon, S. Mu, F. Körmann, Y. Ikeda, C. C. Tasan, D. Raabe, T. Egami, and E. S. Park, Nat. Commun. **10**, 2090 (2019).

[84] X. Zhou, A. Tehranchi, and W. A. Curtin, Phys. Rev. Lett. **127**, 175501 (2021).

[85] N. L. Okamoto, K. Yuge, K. Tanaka, H. Inui, and E. P. George, AIP Adv. **6**, 125008 (2016).

[86] Z. Li and D. Raabe, JOM **69**, 2099 (2017).

[87] Y. Zhao and T. Nieh, Intermetallics **86**, 45 (2017).

[88] W. G. Nöhring and W. Curtin, Scr. Mater. **168**, 119 (2019).

[89] X. Yang, Y. Xi, C. He, H. Chen, X. Zhang, and S. Tu, Scr. Mater. **209**, 114364 (2022).

[90] W. Feng, Y. Qi, and S. Wang, Metals **7**, 482 (2017).

[91] R. Chen, T. Xie, B. Wu, L. Weng, H. Ali, S. Yang, Y. Zhao, P. Zhao, C. Zhang, R. Cao, J. Wen, Q. Yao, Q. Cai, H. Zhang, B. Sa, C. Wen, M. Lin, X. Sun, H. Su, Y. Liu *et al.*, J. Alloys Compd. **935**, 168016 (2023).

[92] J. W. Morris Jr., D. M. Clatterbuck, D. C. Chrzan, C. R. Krenn, W. Luo, and M. L. Cohen, Mater. Sci. Forum **426-432**, 4429 (2003).

[93] G. A. Landrum and R. Dronskowski, Angew. Chem. Int. Ed. **39**, 1560 (2000).

[94] R. Hoffmann, *Solids and Surfaces: A Chemist's View of Bonding in Extended Structures* (Wiley, New York, 1991).
[95] U. Mizutani, in *Surface Properties and Engineering of Complex Intermetallics* (World Scientific, Singapore, 2010), pp. 323–399.
[96] D. Li, P. Hu, M. Meng, H. W. Li, S. X. Wu, and S. W. Li, Mater. Res. Bull. **101**, 162 (2018).
[97] M. Sturza, S. Daviero-Minaud, M. Huvé, N. Renaut, N. Tiercelin, and O. Mentré, Inorg. Chem. **50**, 12499 (2011).
[98] W. Zhong, Y. Yang, S. Hayakawa, H. Xu, K. An, I. Stinson, A. Borisevich, J. Cicotte, and E. George, Int. J. Plast. **167**, 103663 (2023).
[99] P. Chowdhury, H. Sehitoglu, W. Abuzaid, and H. Maier, Int. J. Plast. **71**, 32 (2015).
[100] W. Xu, Z. Xiong, Z. Li, X. Gao, W. Li, T. Yang, X. Li, L. Vitos, and C. Liu, Int. J. Plast. **158**, 103439 (2022).
[101] X. J. Li, S. Schönecker, L. Vitos, and X. Q. Li, Intermetallics **145**, 107556 (2022).
[102] Z. H. Jin, S. T. Dunham, H. Gleiter, H. Hahn, and P. Gumbsch, Scr. Mater. **64**, 605 (2011).
[103] S. Lu, X. Sun, Y. Tian, X. An, W. Li, Y. Chen, H. Zhang, and L. Vitos, PNAS Nexus **2**, pgac282 (2023).
[104] M. Jo, Y. M. Koo, B. J. Lee, B. Johansson, L. Vitos, and S. K. Kwon, Proc. Natl. Acad. Sci. USA **111**, 6560 (2014).
[105] S. Huang, H. Huang, W. Li, D. Kim, S. Lu, X. Li, E. Holmstrom, S. K. Kwon, and L. Vitos, Nat. Commun. **9**, 2381 (2018).
[106] P. J. H. Denteneer and W. Van Haeringen, J. Phys. C: Solid State Phys. **20**, L883 (1987).
[107] M. Olsson, Thermodynamic modeling of the stacking fault energy in austenitic stainless steels, M.S. thesis, KTH Royal Institute of Technology, Stockholm, 2014.
[108] V. Wang, N. Xu, J. C. Liu, G. Tang, and W. T. Geng, Comput. Phys. Commun. **267**, 108033 (2021).
[109] M. A. Caro, S. Schulz, and E. P. O'Reilly, J. Phys.: Condens. Matter **25**, 025803 (2013).